Chapter 9
Coronal Loops

9.1 Coronal Loops: Stereoscopy and 3-D Geometry

The most ubiquitous structures in the solar corona are *loops*, often appearing with approximately semi-circular geometry, obviously representing visible manifestations of closed magnetic field lines. The magnetic field is not directly visible in any wavelength, but our knowledge of its topology and geometry is based on our understanding that some field-aligned coronal structures become filled with hot plasma that radiates in EUV and soft X-rays, and this way illuminates selected bundles of magnetic field lines. The super-position of myriads of illuminated loops in multi-polar active regions can lead to EUV and soft X-ray images with fairly complex topology, but in principle can be rendered with a suitable 3-D magnetic field model and hydrostatic 1-D loop models for each field line, as demonstrated for active regions observed with SXT/Yohkoh (Gary 1997; Lundquist et al. 2008), or with full-Sun visualizations (Schrijver et al. 2004).

A number of exercises have been conducted to adjust a theoretical magnetic field model to the observed 2-D projections of coronal loops, such as radial stretching of a potential field (Gary and Alexander 1999), varying the α-parameters in linear force-free field models (Wiegelmann and Neukirch 2002), forward-fitting of a series of submerged dipoles (Sandman and Aschwanden 2011), or varying the α-parameters in vertical current approximations of nonlinear force-free fields (Aschwanden 2013). What became clear even in the pre-STEREO era is that the 3-D geometry of observed coronal loops is not consistent with potential fields, as demonstrated for a sample of $\approx$ 60 loops in an active region observed with SOHO/EIT and reconstructed with the solar-rotation stereoscopy method (Aschwanden et al. 1999, 2000).

The launch of STEREO in 2006 augmented previous solar rotation-based methods with a new opportunity to conduct true stereoscopy, performed with two identical spacecraft with a suitable separation angle. The very first results from EUVI/STEREO/A and B reported the triangulation of $\approx$ 50 loops viewed at a

M. J. Aschwanden, *New Millennium Solar Physics*, Astrophysics and Space Science Library 458, https://doi.org/10.1007/978-3-030-13956-8_9

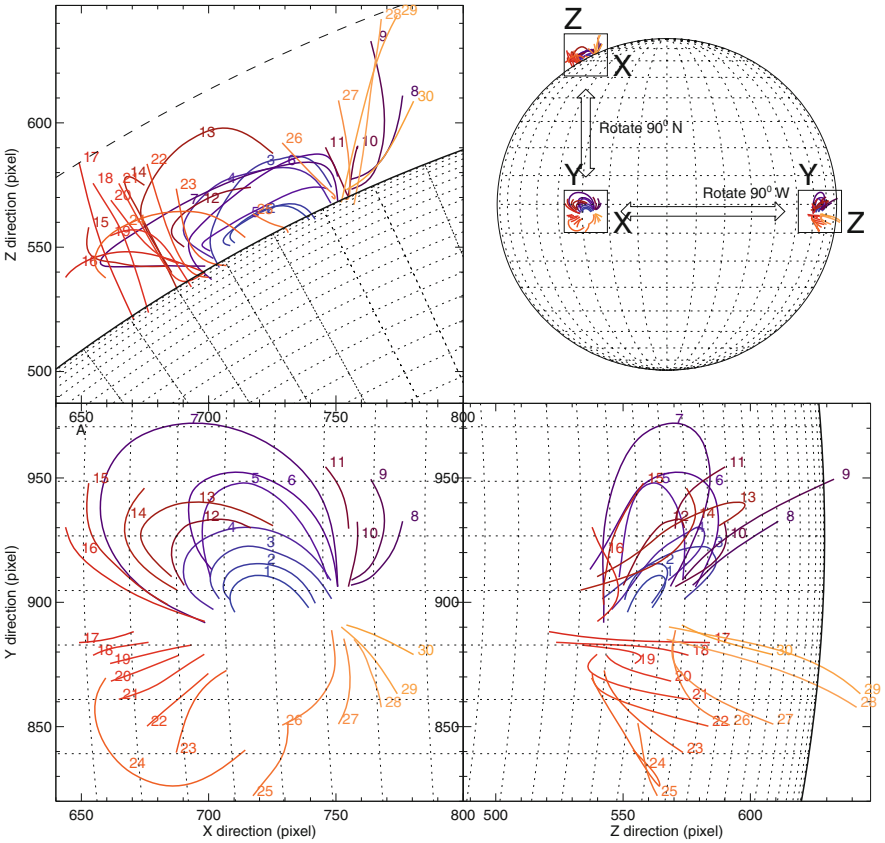

Fig. 9.1 3-D representation of 30 stereoscopically triangulated loops observed with EUVI/STEREO/A and B on 2007 May 9: in the XY plane (bottom left); in the ZX plane or rotated by 90° to the west (bottom right); and in the XZ plane, rotated by 90° to the north (top left). A synopsis of the rotations of the three perspectives is shown in the top right frame (Aschwanden et al. 2008)

spacecraft separation angle of $\approx$ 12° (Feng et al. 2007). The stereoscopic 3-D geometry of only $\approx$ 10 (out of 50) loops could locally be modeled with a linear force-free model, while no model could fit all triangulated loops, leading to the conclusion that linear force-free models are not adequate to explain the observed 3-D geometry of active region loops. Somewhat earlier on, when the STEREO/A and B had a spacecraft separation angle of 7°, a number of 30 loop structures (7 complete and 23 partial segments) were stereoscopically triangulated (Fig. 9.1), yielding the height range, stereoscopic height measurement errors, the loop plane inclination angles, and measurements of the coplanarity and circularity of the loops (Aschwanden et al. 2008). The loops were found to have large inclination angles from the vertical ($\theta \approx 36°–73°$), curvature radius variations of 3%–30%, and deviations from planarity by 3%–13% of the loop baselines (Fig. 9.2). The

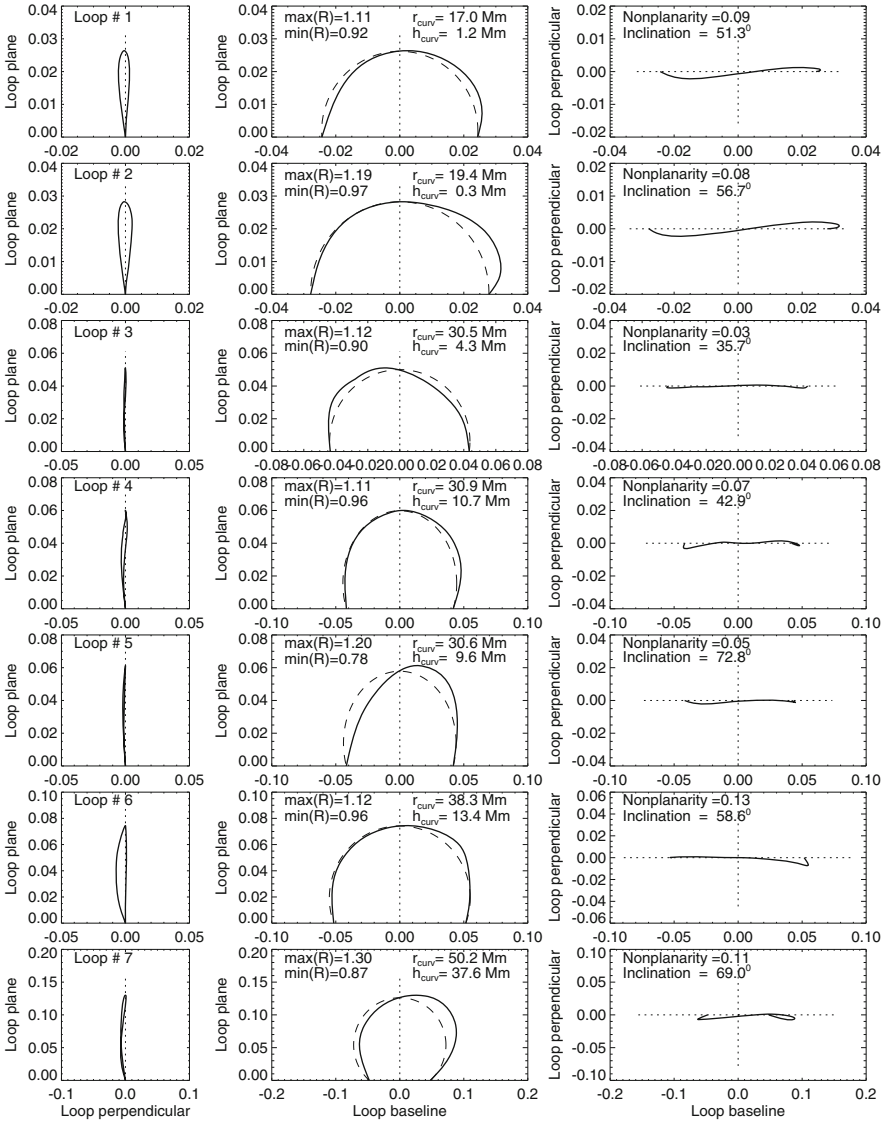

Fig. 9.2 Projections of 7 complete loops (of the same set as shown in Fig. 9.1) are shown in the loop plane (middle panels) and in orthogonal directions, from the side (left panels), and from top (right panels). The loop plane is defined by the two footpoints and the loop top above the midpoint between the footpoints. A circle is also interpolated through these 3 points in order to visualize the circularity (dashed linestyle). Note the deviations from coplanarity in the side view (left panel) and top view (right panel) (Aschwanden et al. 2008)

knowledge of the exact 3-D geometry of a loop with respect to the observers line-of-sight has important consequences for determining the correct vertical density scale height (used in hydrostatic models), the aspect angle of loop cross-sections (used in inferring electron densities from optically thin emission measures), the absolute flow speeds (used in siphon flow models), the correct loop length (used in loop scaling laws), as well as the 3-D vectors of the coronal magnetic field (used in testing theoretical magnetic field extrapolation models). Extreme deviations from a semi-circular geometry were found in oscillating loops, which appear to have strong helical twist (Aschwanden 2009). Stereoscopic triangulation of coronal loops is feasible from small ($\gtrsim 6°$) to large angles ($\lesssim 170°$) of the spacecraft separation, but the ambiguity in the identification of corresponding loop pairs becomes more severe for large angles $\gtrsim 30°$ (Aschwanden et al. 2012).

Statistics of geometric parameters is useful for testing physical scaling laws. For coronal loops, which often ressemble slender long structures, we can measure their length L and their width w. The loop lengths range from the smallest detectable size of $L_{min} \approx 1$ Mm to the size of the largest active region, $L_{max} \lesssim 250$ Mm, so they cover at least two orders of magnitude in scale, generally outlining incomplete segments of magnetic field lines.

9.2 Coronal Loops: Cross-Sectional Widths

The reduction from 3-D to 1-D hydrodynamics in coronal loops requires the definition of a cross-sectional dependence of a flux tube area $A(s)$ as a function of the loop length coordinate s, which is assumed to be constant in the simplest case. Another fundamental assumption is the monolithic structure of coronal loops, which is likely to break down for large loop widths. It is therefore imperative to measure the width of coronal loops with high-resolution instruments and to test their homogeneity (in the case of monolithic loops) or inhomogeneity (in the case of multi-stranded loops).

Cross-sectional widths of coronal loops have been measured with many different instruments (Dunn/SacPeak, Pic du Midi, Skylab, NRAO, VLA, ASE rocket, CSIRO, LMSAL rocket, SXT/Yohkoh, EIT/SOHO, TRACE, EIS/Hinode, CRISP, AIA/SDO, Hi-C, SOT/Hinode, IRIS) and wavelengths (optical, Hα, Lyα, EUV, soft X-rays, and radio). A compilation of 53 studies on loop width measurements is depicted in Fig. 9.3, showing the loop widths (on the x-axis) sorted by increasing widths (on the y-axis). The numbered references are listed in the original paper (Aschwanden and Peter 2017), from which we cite the most recent ones with the highest spatial resolution only (after 2010): Aschwanden and Wülser (2011 [37]); Aschwanden and Boerner (2011 [38]); Aschwanden and Schrijver (2011 [39]); Aschwanden et al. (2013 [43]); Mulu-Moore et al. (2011 [40]); Brooks et al. (2012 [41], 2013 [45], 2016 [51]); Antolin and Rouppe van der Voort (2012 [42]); Peter et al. (2013 [44]); Winebarger et al. (2013 [46], 2014 [49]);

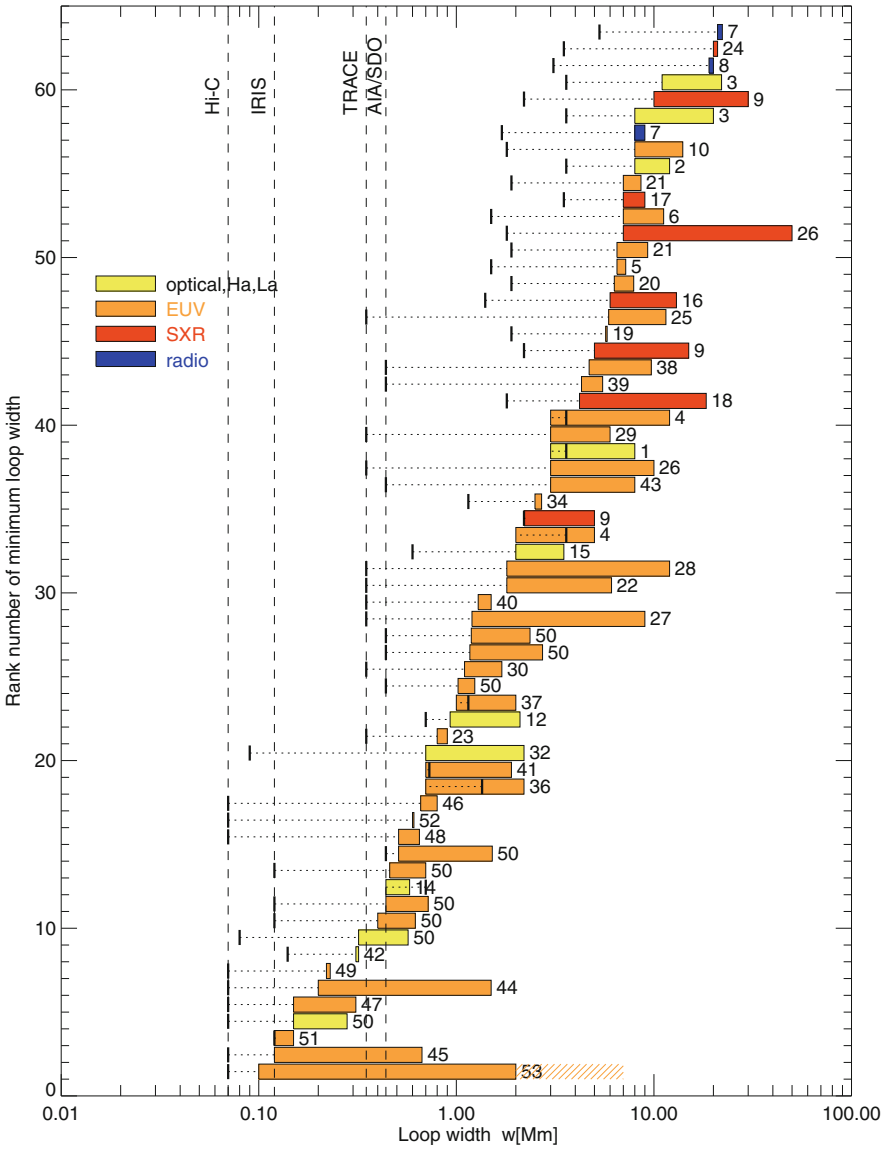

Fig. 9.3 Compilation of loop width measurements from literature during 1963–2017: The measured ranges are represented by blocks, colored by wavelength regimes (yellow=optical, Hα, Lα; orange=EUV, red=SXR, and blue=radio), labeled with the reference number cited in the text, and sorted by the increasing minimum width on the y-axis. The instrumental pixel size (or resolution if pixel size is not known) is indicated with a black thick bar for each measurement (adapted from Aschwanden and Peter 2017)

Morton and McLaughlin (2013 [47]); Alexander et al. (2013 [48]); Antolin et al. (2015 [50]); Tiwari et al. (2016 [52]); Aschwanden and Peter (2017 [53]).

The graphical representation in Fig. 9.3 divides the loop width measurements into 4 wavelength regimes by color (optical + Hα + Lyα, EUV, soft X-rays, and radio), and ranks the width ranges by the smallest detected width in ascending order. There are several trends visible in Fig. 9.3. Minimum loop widths have been measured from $w \approx 20$ Mm down to $w_{min} \approx 0.1$ Mm. The finest loop widths have been detected preferentially in EUV, while the loop widths measured in soft X-rays and optical wavelengths tend to be significantly larger, and are found to be largest in radio wavelengths. Since coronal loops in EUV and soft X-rays are produced by optically thin line emission, the density contrast of individual loops is much "crisper" than in structures detected in the optically thick regime of free-free and gyroresonance emission in radio wavelengths.

In Fig. 9.3 we can see also that the smallest loop widths are typically measured approximately at 2–4 pixels above the instrumental pixel sizes, which is partially explained by the point spread function that typically amounts to $w_{psf} \approx 2.5$ pixels in most EUV imagers (TRACE, AIA/SDO, STEREO, IRIS, Hi-C). Some additional scatter in the order of $w_{noise} \approx 1$ pixel is due to the noise in the background subtraction, so that the observed loop width w is broadened by,

$$w \approx \sqrt{w_{true}^2 + w_{psf}^2 + w_{noise}^2} \,, \tag{9.2.1}$$

if we add the uncertainties in quadrature. We may ask whether the distribution of loop sizes continues at the low end, if future instruments faciliate higher spatial resolutions. However, several studies with the highest available spatial resolution, with a pixel size of $w_{pixel} \approx 0.1'' \approx 70$ km for the Hi-C instrument, have demonstrated that AIA resolves many of the loops, as shown in Fig. 9.4. The smallest loops measured from recent Hi-C studies cover ranges of $w = 200$–1500 km (Peter et al. 2013), $w = 117$–667 km (Brooks et al. 2013), $w = 150$–310 km (Morton and McLaughlin 2013), $w = 120$–150 km (Brooks et al. 2016), with a most frequent width of $w \approx 500$ km (Aschwanden and Peter 2017).

There is no widely accepted theoretical model for the cross-sectional widths of coronal loops. The intrinsic loop widths supposedly reveal the cross-sectional area over which energy is deposited in a magnetic flux tube during an elementary heating event. However, since the basic coronal heating mechanism is still elusive, one can not predict the range of loop widths. Parker's nanoflare scenario envisions unresolved loop strands, while heating mechanisms with cross-field diffusion in a high-β regime predict monolithic resolved loops (Fig. 8.8). If the latest Hi-C measurements with finite loop widths with a most frequent value of $w \approx 500$ km hold up, we have to conclude that nanoflare strands with widths $w \lesssim 500$ km are negligible in the energy budget of the heating process. The particular value of $w \approx 500$ km apparently demarcates two types of granulation in the solar photosphere: the mini-granulation with a width range of $w \approx 100$–600 km (Abramenko et al. 2012), and the regular granules which have a Gaussian distribution with a mean of $w \approx 1000$ km.

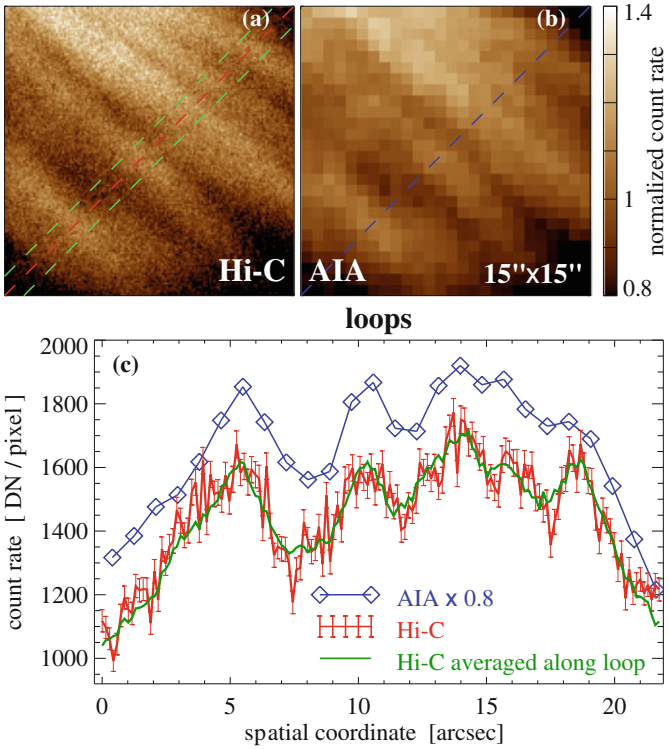

Fig. 9.4 Hi-C 193 Å observations with a pixel size of 0.1″ (**a**), compared with AIA 195 Å observations with a pixel size of 0.6″ (**b**), and cross-sectional profiles (**c**), across a bundle of loops (hashed diagonal lines in top panels). Note that 4–5 loop structures are fully resolved with AIA, while Hi-C shows data noise without additional significant fine structure (from Peter et al. 2013)

9.3 Coronal Loops: Multi-Strand Structure

Hydrodynamic modeling of coronal loops during the last two decades has been generalized from a single flux-tube concept to a multi-stranded macroscopic loop system, which has a number of consequences: (1) the observed macroscopic loops may indeed consist of finer unresolved strands, in particular for instruments with poor spatial resolution, which makes the measured physical parameters instrument-dependent (Fig. 9.5); (2) modeling a multi-stranded loop system introduces additional degrees of freedom (such as filling factors) that makes the interpretation of observables more ambiguous; and (3) the discrimination between homogeneous (monolithic) single loops and the inhomogeneous (multi-stranded) loop systems is tied to macroscopic versus microscopic coronal heating mechanisms, similar to the dichotomy between large-scale flares (for which we resolve the magnetic reconnection geometry) and nanoflares (which we do not resolve). Observationally, the majority of loops measured with arcsecond resolution instruments (TRACE, AIA)

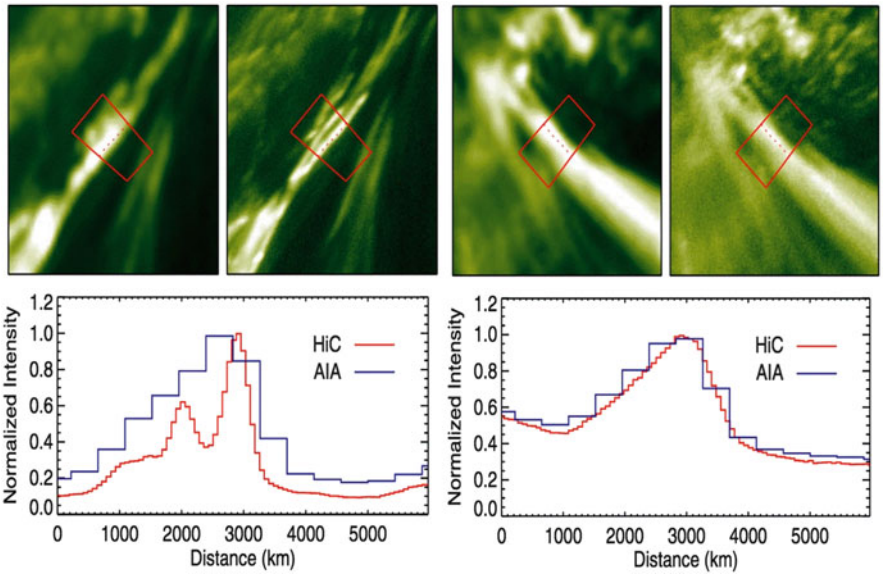

Fig. 9.5 Examples of a multi-strand loop that is resolved with Hi-C but not with AIA (left panels) and a monolithic loop that is fully resolved with both Hi-C and AIA (right panels). For each case, the AIA and Hi-C images at 193 Å are shown, along with intensity profiles (Brooks et al. 2013)

were found to be isothermal (Aschwanden and Nightingale 2005), which is consistent with resolved single loop strands, rather than with multi-stranded loop structures (unless all strands have the same temperature).

Let us review a few lessons we learned from multi-strand loop modeling and observations. The flat temperature profile along coronal loops can be reproduced by both a footpoint-heated monolithic loop or by an ensemble of uniformly heated loops (Reale and Peres 2000), as well as by an ensemble of footpoint-heated loops (Mendoza-Briceno et al. 2002). The discrepancy between the observed decay times of warm loops and the theoretical lifetime inferred from time-dependent hydrostatic simulations can be reconciled with a multi-strand system (Fig. 9.6), while it fails for most monolithic loops (Warren et al. 2002, 2003). Electron density and temperature diagnostics does not discriminate between the spatial form of the heating function in multi-strand (nanoflare) hydrodynamic simulations (Patsourakos and Klimchuk 2005; Sarkar and Walsh 2008, 2009). The temperature of the cold corona ($T_e \approx 1.0$–1.5 MK) as well as the fuzziness of the warm corona ($T_e \approx 2$–3 MK) can be reproduced with nanoflare simulations in a multi-strand corona (Reale et al. 2005, 2011; Guarrasi et al. 2010). Multi-strand hydrodynamic simulations produce modest line broadening (e.g., Ne VII and Mg X) that is consistent with observations (Patsourakos and Klimchuk 2006; Taroyan et al. 2006). Nonthermal widths of hot loops (1–4 MK) measured in non-flaring regions did reveal only small nonthermal velocities ($v = 17.6 \pm 5.3$ km s^{-1}) (Brooks et al. 2016).

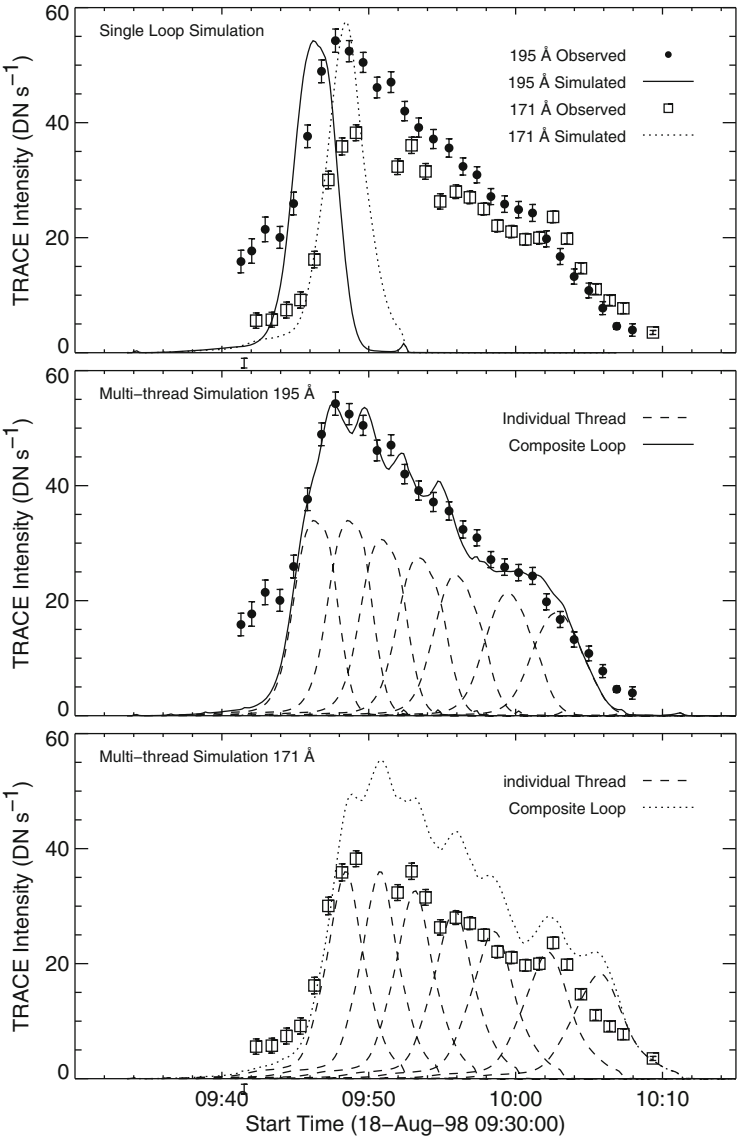

Fig. 9.6 Simulated and observed light curves for the TRACE active region loop observed on 1998 August 18. *Top:* Simulated light curve for a single loop. The delay between the 195 and 171 Å intensities in the simulated light curve matches the observations, but the loop cools too quickly. *Middle and Bottom:* Simulated light curve for a series of threads that are heated sequentially. The initial thread matches the observed delay. Subsequent threads have the same heating duration but smaller peak heating rates (Warren et al. 2003)

Multi-stranded loop models cannot reproduce both the transition region DEM distribution and the coronal DEM distribution with a unique set of parameters (Susino et al. 2010, 2013; Reale and Ciaravella 2006; Winebarger et al. 2011; Mulu-Moore et al. 2011). Hi-C observations (Fig. 9.4) over-resolve some single loops, which have cross-sectional widths of $w \approx 100$–500 km (Peter et al. 2013), implying that most loops with a width of $w \gtrsim 500$ km are likely to be composite or multi-stranded loops (Aschwanden and Peter 2017). Other nanoflare simulations determine filling factors (Jain and Yashiro 2002), spontaneous current sheets in filamentary loop systems (Petrie 2006), statistical models of the inhomogeneous corona (Aschwanden et al. 2007), the effects of filter-ratio analysis on the flat temperature profile in multi-stranded loop models (Bourouaine and Marsch 2010), the multi-thermal and multi-stranded nature of coronal rain (Antolin et al. 2015), or the effects of low-frequency versus high-frequency nanoflare heating (Bradshaw and Klimchuk 2015).

9.4 Coronal Loops: Cross-Sectional Temperature

The 1-D flux tube concept of a coronal loop in principle implies a homogeneous electron pressure, density, and temperature across the loop cross-section. In order to verify the cross-sectional temperature structure of coronal loops, multi-wavelength images observed with EIT/SOHO, TRACE, and AIA/SDO have been analyzed in great detail. The main question focused on the discrimination between monolithic (isothermal) and unresolved multi-stranded (multi-thermal) loop cross-sections. Monolithic (macroscopic) loops are by definition homogeneous in temperature and density across their cross-section, and thus require cross-field transport of plasma from a heating source that is spatially resolved with current instrumentation. In contrast, multi-stranded loop cross-sections are inhomogeneous in temperature and density. They display a broad multi-temperature (differential emission measure) distribution, because the unresolved strands are independently heated by microscopic heating sources, as envisioned in the original nanoflare heating scenarios.

How is the temperature structure measured across a coronal loop or multi-stranded loop system ? In the simplest method, a loop segment has to be identified in an image data set with (n_λ) multiple wavelengths, which yields a set of fluxes $F_i, i = 1, \ldots, n_\lambda$ to which a differential emission measure (DEM) analysis is applied (see Sect. 2.6 and Table 2.3 for an overview of different DEM methods). The outcome of the DEM analysis yields then either a narrow ($\Delta T/T$) $\ll 1$ or a broad DEM distribution ($\Delta T/T \approx 1$). Narrow temperature peaks indicate a near-isothermal structure, while broad DEMs imply a multi-thermal distribution. There are a number of systematic effects that can make the results ambiguous. For instance, if an instrument has a poor spatial resolution, a bundle of closely-spaced loop strands appear as a single loop, which constitutes a strong bias for a broad multi-thermal structure. Moreover, if a loop is observed near or beyond the limb, the observed loop flux is likely to be contaminated by large foreground and

background fluxes, which creates a bias for broad multi-thermal structures, since the target loop and the background are likely to have different temperatures. Therefore, clean results depend very much on the availability of high-resolution instruments, an accurate DEM inversion method, and careful background modeling. A selection of results on the thermality of loop cross-sections is provided in Table 9.1.

Table 9.1 Measurements of isothermal ($\sigma_T = \Delta T/T \lesssim 0.1$) and multi-thermal coronal loop cross-sections. The number of widths specifies how many loop (or thread) widths have been measured in each reference

Instrument	Wavelengths Å	Number of widths	Temperature range	Ref.
CDS, SXT	310–380, 517–633	13	Isothermal, multi-thermal	[1]
TRACE	171, 195	200	Isothermal, multi-thermal	[2]
SUMER, SXT	660–1600	45	Near-isothermal	[3]
CDS, TRACE	173	5	Isothermal	[4]
CDS, TRACE	173, 195	5	Near-isothermal	[5]
XDT, SXT, EIT, CDS	210–213,171,195,284	9	Multi-thermal	[6]
EIT, SUMER	668–1463	5	Isothermal	[7]
EIT	171, 195, 284	50	...	[8]
CDS	310–380, 517–633	3	Multi-thermal	[9]
TRACE	171, 195, 284	3500	Isothermal (84%)	[10]
CDS, EIT	150–785	3	Multi-thermal	[11]
CDS, TRACE	150–785	10	Isothermal	[12]
CDS	150–785	2	Isothermal, multi-thermal	[13]
EIS	171–212, 245–291	20	Near-isothermal	[14]
EIS	171–212, 250–290	1	Multi-thermal	[15]
SUMER	500–1600	3	Near-isothermal	[16]
EIS	170–210, 250–290	2	Near-isothermal	[17]
CDS, TRACE	171, 195, 284	2	Isothermal, multi-thermal	[18]
XRT, EIS	170–210, 250–290	5	Multi-thermal	[19]
AIA	94,131,171,193,211,335	1	Multi-thermal	[20]
AIA	94,131,171,193,211,335	12	Multi-thermal	[21]
EIS, XRT	186–274	1	Multi-thermal	[22]
AIA	94,131,171,193,211,335	12	Isothermal, multi-thermal	[23]
AIA	94,131,171,193,211,335	100	Isothermal (66%)	[24]
AIA	94,131,171,193,211,335	6	Near-isothermal	[25]
AIA	94,131,171,193,211,335	2892	$\sigma_T = 0.24 \pm 0.20$	[26]
AIA	94,131,171,193,211,335	12	Isothermal, multi-thermal	[27]

References: Schmelz (2002) [1]; Schmelz et al. (2001 [1], 2003 [8], 2005 [9], 2007 [13], 2008 [15], 2009 [18], 2010a [19], 2010b [20], 2011a [21], 2011b [22], 2011c [23], 2013 [27]); Testa et al. (2002) [2]; Warren and Warshall (2002) [3]; Del Zanna (2003) [4]; Del Zanna and Mason (2003) [5]; Nagata et al. (2003) [6]; Warren and Winebarger (2003) [7]; Aschwanden and Nightingale (2005) [10]; Schmelz and Martens (2006) [11]; Cirtain et al. (2007) [12]; Warren et al. (2008) [14]; Landi and Feldman (2008) [16]; Tripathi et al. (2009) [17]; Aschwanden and Boerner (2011) [24]; Brooks et al. (2011) [25]; Aschwanden et al. (2013) [26]

A number of criticisms have been raised concerning the various used DEM analysis methods, such as: (1) over-restricted temperature range, i.e., EIT with $T \approx$ 1–2 MK (Schmelz et al. 2003); (2) atomic lines missing in the CHIANTI code, e.g., in the 94 Å band (Aschwanden and Boerner 2011; Del Zanna 2013; Landi and Klimchuk 2010); (3) insufficient spatial resolution, i.e. CDS/SOHO data with a point-spread function of $6'' \times 8''$ (Schmelz 2002; Schmelz et al. 2001, 2003, 2005, 2007, 2009; Del Zanna 2003; Del Zanna and Mason 2003; Cirtain et al. 2007); (4) the ambiguity of the 2-filter-ratio technique (Weber et al. 2005; Martens et al. 2002); (5) the lack of background subtraction (Schmelz et al. 2001; Schmelz 2002); (6) over-smoothing of the fitted DEM function (Schmelz et al. 2001; Aschwanden 2002; Landi and Feldman 2008); (7) isothermal bias for over-estimates of the photometric uncertainty (Patsourakos and Klimchuk 2007); or (8) the choice of the radiative loss function (Reale and Landi 2012; Sasso et al. 2012). What matters additionally is the dynamical condition of a loop: quiescent active region loops often exhibit a narrow (near-isothermal) DEM (if they are spatially resolved), while flaring loops tend to exhibit broadband (multi-thermal) DEMs (e.g., Warren et al. 2013). A statistical rule-of-thumb was found that elementary loop strands: (i) are near-isothermal ($\Delta T \lesssim 0.2$ MK), (ii) have a small width ($w \leq 2$ Mm), and (iii) have a faint contrast ($\lesssim 30\%$) (Aschwanden 2005). Comparing the 27 studies listed in Table 9.1 it appears that isothermal (or near-isothermal) loops are more likely to be detected at "warm coronal temperatures" ($T \approx$ 1–2 MK), using instruments with the highest spatial resolution (TRACE with $0.5''$ and AIA with $0.6''$ pixels), and after proper background subtraction. Loops or multi-strand loop systems are also detected at hotter (flare-like) temperatures ($T \approx$ 3–30 MK), with instruments that have soft X-ray coverage (SXT, CDS, EIS, XRT). However, since these instruments have a relatively poor spatial resolution and often were analyzed without background subtraction, we can not decide whether hot loops are isothermal or multi-thermal.

9.5 Coronal Loops: Flows

Plasma flows in coronal loops require a generalization of static models (with velocity $v = 0$) in the 1-D hydrodynamic equations, enabling the calculation of simple steady-flow solutions ($v = const$), as well as siphon-flow solutions, which are driven by a pressure imbalance between the loop footpoints. An essential feature of steady flow solutions is their acceleration with increasing height (because the electron density decreases due to gravitational stratification and momentum conservation), which can exceed the sound speed and become supersonic and form stationary shocks. There is a wealth of flow patterns that can occur in the solar corona, such as blueshifted upflows, redshifted downflows, siphon flows, turbulent flows, shocks generated by critical or supersonic flows, reconnection inflows, reconnection outflows, etc. In the following we will review new measurements (Table 9.2) and hydrodynamic modeling after 2000, which were mostly obtained with EIS/Hinode and AIA/SDO.

Table 9.2 Flow measurements in the solar corona ($T \approx 0.5$–3.0 MK) after 2000

Observer	Instrument	Wavelength Å	Temperature T_e [MK]	Flow speed v (km s^{-1})
Winebarger et al. (2002)	SUMER, TRACE	780–1610	0.6–2.0	15–40
Feldman et al. (2003)	SUMER	780–1610	2.6–6.6	20–35
Singh et al. (2005)	NOGIS	5303, 6374	0.7	48
Brosius (2005)	CDS, EIT	171–629	0.2–2.0	15–25
Brosius and Landi (2005)	CDS, EIT	171–629	0.2–2.0	52
Doyle et al. (2006)	TRACE, SUMER	171, 1550	0.2–1.0	120
Hara et al. (2008)	EIS	166–211, 246–291	2.0	10–30
Doschek et al. (2008)	EIS	166–211, 246–291	1.2–1.4	20–50
Del Zanna (2008)	EIS	166–211, 246–291	1.0–3.0	5–30
Tripathi et al. (2009)	EIS	166–211, 246–291	1.0–2.0	<60
Warren et al. (2011)	EIS	166–211, 246–291	0.4–2.2	<40
Raju et al. (2011)	Fabry-Perot	5303	1.8–3.1	20–40
Ugarte-Urra and Warren (2011)	EIS	166–211, 246–291	0.6–1.0	40–130
McIntosh et al. (2012)	EIS, AIA	166–211, 246–291	< 1	10, 50–150
Tripathi et al. (2012a)	EIS, AIA	166–211, 246–291	0.6–1.6	4–20
Tripathi et al. (2012b)	EIS, AIA	166–211, 246–291	0.6–1.6	0±5
Su et al. (2012)	AIA,SOT,EIS	171, 304, 3968	1.0–3.0	80–200
Orange et al. (2013)	EIS	171–212, 250–290	0.6–1.0	5–60
Baker et al. (2017)	EIS	171–212, 250–290	0.6–1.0	11–32

The interpretation of the Dopplershift of flows depends very much on the heliographic position. Near disk center we expect a maximum blueshift for upflows, which should vanish when seen near the limb. Such a center-to-limb pattern in the directivity was indeed observed in upflows ($v \approx 20$ km s^{-1}) near the footpoints of active region loops with EIS/Hinode (Hara et al. 2008; Doschek et al. 2008), persistent for at least a day (Doschek et al. 2008), and extending into the heliosphere and solar wind (Doschek et al. 2008). The center-to-limb variation introduces systematic changes in the line shift, from which the inclination and angular spread can be measured (Démoulin et al. 2013; Baker et al. 2017). Besides persistent blueshifted upflows (Patsourakos et al. 2014), persistent redshifts were observed near loop footpoints in active regions too (Del Zanna 2008). This apparent co-spatial co-existence of blueshifted outflows and redshifted downflows was disentangled as two different temperature regimes: redshifted emission at transition region temperatures and blueshifted emission at coronal temperatures (Tripathi et al. 2009; Warren et al. 2011; Kamio et al. 2011). This dichotomy of flows was called *"coronal contra-flow"* or *"chromosphere-corona mass cycle"* (McIntosh et al. 2012). The emission in the blue wing was found to propagate upward fast ($v = 50$–150 km s^{-1}) and to contribute a few percents to the total emission only, while the *"draining"* of cooler material descends slowly ($v \approx 10$ km s^{-1}) while radiatively cooling (McIntosh et al. 2012), forming a complex near-cospatial mass cycle. Upflows with

velocities of $v = 48$ km s^{-1} forming loops with life times of 4 hrs were also observed in optical wavelengths (Singh et al. 2005). Strong blueshifts of $v \approx 20$–40 km s^{-1} were measured in the solar corona during a total eclipse (Raju et al. 2011). Other velocity measurements in upflows and downflows were reported also by Brosius (2005), Brosius and Landi (2005), Tripathi et al. (2012a), Orange et al. (2013), Kano et al. (2014), see compilation in Table 9.2. Most of the observed upflow events have been interpreted as a result of a local magnetic reconnection process that triggers chromospheric evaporation. Using magnetic extrapolations in the upflow regions, it was found that flows occur in thin, fan-like structures rooted in quasi-separatrix layers, between over-pressure active region loops and neighboring under-pressure loops (Démoulin et al. 2013).

On the theoretical side, 1-D hydrodynamic simulations have been carried out to calculate steady-flow solutions, but observational evidence is scarce. It was found that a sufficiently large heating asymmetry can produce the observed loop over-density (Winebarger et al. 2002), but very short pressure scale heights are needed, so that most of the warm ($T = 1$–2 MK) EUV loops cannot be explained by flows (Patsourakos et al. 2014). A transient motion along a cool loop observed with TRACE and SUMER has been modeled in terms of a siphon flow model, but the transient lasted only a few minutes, which is much shorter than expected for quasi-steady siphon flows (Doyle et al. 2006). The observed flows in a loop structure located in the penumbra of a sunspot were found to match theoretical predictions of chromospheric and coronal siphon flows, with accelerating upflowing plasma at one footpoint with low field strength and decelerating downflowing plasma at the other end (Fig. 9.7), possibly forming a tube shock (Bethge et al. 2012). High-velocity

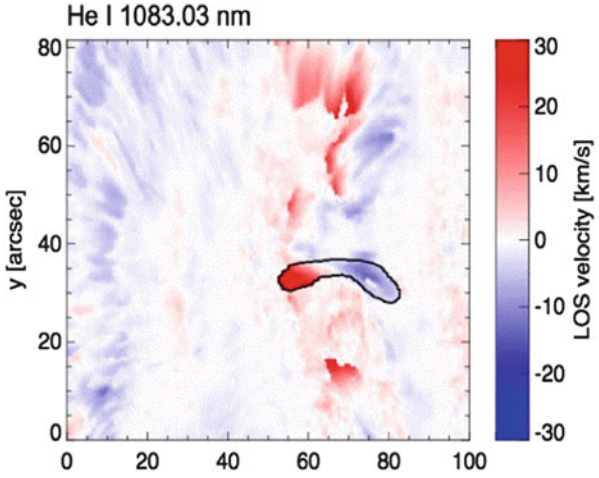

Fig. 9.7 Line-of-sight velocities (upflows in blueshift and downflows in redshift) observed in the He I line (10,830 Å) of a cool loop rooted in the penumbra of a sunspot, observed with TIP/VTT, Tenerife (Bethge et al. 2012)

flows can be generated by the generalized magneto-Bernoulli mechanism (Mahajan et al. 2002). Multi-species hydrodynamic simulations show the Coulomb coupling of the electrons and ions induces drag that counteracts the tendency of ions to settle into gravitational stratification (Lenz 2004). Ions and protons couple well in the line-forming region (Byhring et al. 2008). The coronal helium is found not to *"drain"*, leading to extreme increases of the helium abundance from the upper chromosphere to the corona (Killie et al. 2005).

9.6 Coronal Loops: Catastrophic Cooling

Hot coronal loops ($T_e \gtrsim 3$ MK) mostly cool by conductive energy loss, while radiative energy loss dominates later on (in warm loops with $T_e \approx 1$–3 MK). At even lower loop temperatures ($T_e < 1$ MK), radiative losses are no longer balanced by gains through heat conduction or in-situ heating, and therefore the radiatively-driven thermal instability sets in. This phase of the loop evolution is called *"catastrophic cooling"* or *"condensation"*. During this condensation phase, cold plasma blobs collapse and fall from the corona back to the chromosphere, a phenomenon that is also called *"coronal rain"*, which is observed in active regions, post-flare loops, eruptive filaments, and prominences (see examples in Fig. 9.8).

Recent observations of coronal rain with the CRISP instrument at SST in the H-α and Ca II H wavelengths quantify the dynamics (average falling speeds of $v \approx 70$ km s^{-1} and mass drain rate of $dm/dt \approx (1.5\text{–}5) \times 10^9$ g s^{-1}), geometric shapes (average lengths of $L \approx 710$ km and widths of $w \approx 310$ km), trajectories (along the magnetic field, with fall times of $\tau \approx 1$–10 min), and thermodynamic

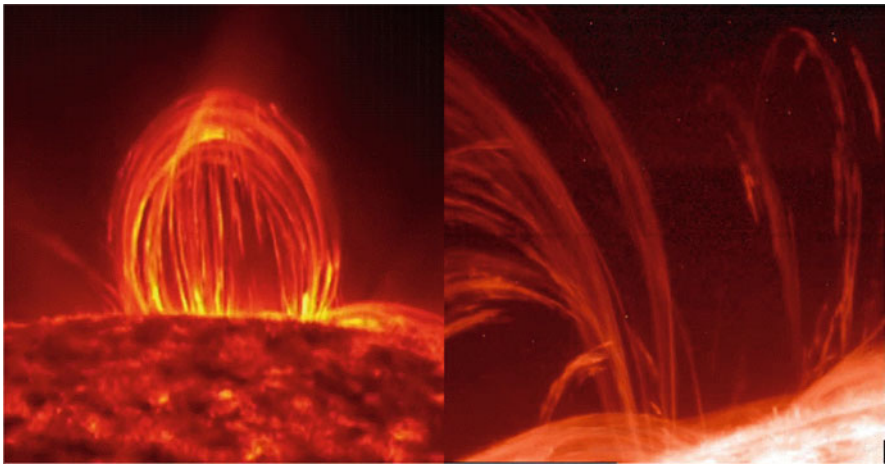

Fig. 9.8 Observations of coronal rain: *Left:* AIA/SDO observations on 2012-07-19 at 304 Å; *Right:* IRIS observations on 2015-03-06, 19:03:29 UT at 2796 Å (Credit: NASA, IRIS Team)

properties (average temperatures $T_e < 7000$ K) and densities ($n_e \approx (0.2\text{–}2.5) \times 10^{11}$ cm^{-3}) of the condensations (Antolin and Rouppe van der Voort 2012; Antolin et al. 2015). The formation of flare-driven coronal rain was observed in 5 phases: heating, evaporation, conductive cooling for ≈ 2 min, radiative enthalpy cooling for 1.3 hrs, and catastrophic cooling during 0.6–2.0 min, leading to rain strands with periods of 55–70 s (Scullion et al. 2016). These measurements confirm that the acceleration is largely below the effective gravity along loops, and that the trajectories follow the coronal magnetic field. The maximum descending speed was found to be correlated with the ratio of electron densities inside and outside the falling blobs (Oliver et al. 2016). While the falling of coronal condensations is easiest observed above the limb, the phenomenon is also found "on-the-disk", with similar physical parameters (Antolin et al. 2012; Ahn et al. 2014), which could explain also part of the ubiquitous redshifts observed on the disk. Combining the CRISP/SST measurements with AIA and IRIS, coronal rain is found to be highly multi-thermal and multi-stranded, with a high degree of co-spatiality in the multi-wavelength (optical and EUV) emissions (Antolin et al. 2015). The funneling effect of the upward diverging magnetic field streamlines the coronal rain into a more continuous and persistent stream at low altitudes, just before it impacts the chromosphere (Antolin et al. 2015).

Recent numerical 1-D hydrodynamic simulations of the condensation of plasma in cool ($T_e < 1$ MK) short loops ($L = 10$ Mm) exhibit a cyclic pattern of chromospheric evaporation, condensation, motion of the condensation region to either side of the loop, and finally loop reheating with a period of 1–2 hrs (Müller et al. 2003). It is found that the radiatively-driven thermal instability occurs about an order of magnitude faster than the Rayleigh-Taylor instability, which can occur in a loop with a density inversion at its apex also (Müller et al. 2003). Simulations with different heating functions reveal that the process of catastrophic cooling is not initiated by a drastic decrease of the total loop heating rate, but rather results from a loss of equilibrium at the loop apex as a natural consequence of (even steady) footpoint heating (Müller et al. 2004; Peter et al. 2012). In the case of repetitive impulsive heating, the cycle period to maintain a short loop at coronal temperatures is very sensitive to the loop length, for instance $T_{cycle} \approx 3$ min for $L = 5\text{–}10$ Mm (Mendoza-Briceno et al. 2002).

Much longer cycles, with periods of $T = 3.8\text{–}9.0$ hrs (lasting over several days), where found in some active region loops, which were interpreted in terms of thermal non-equilibrium evaporation and condensation cycles also (Froment et al. 2015, 2017). The time evolution of plasma temperatures $T(t)$ and emission measure EM, as well as phase diagrams of $T - EM$, are shown in Fig. 9.9 for three cases (with mean periods of 3.8, 5.0, and 9.0 hours).

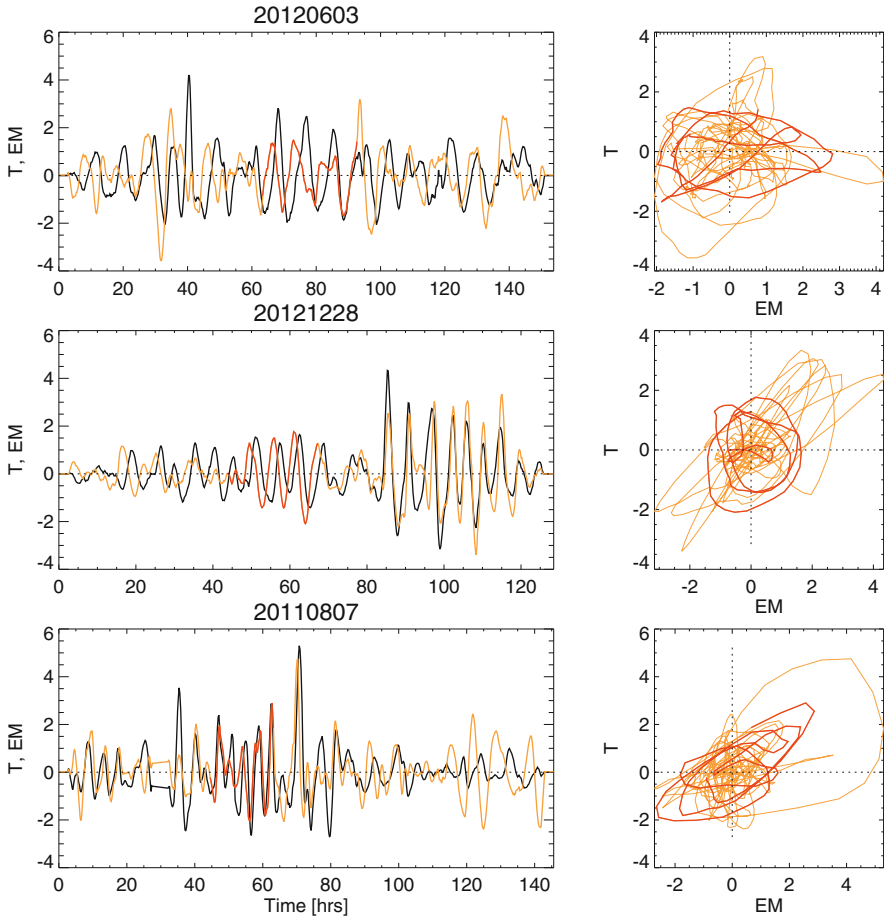

Fig. 9.9 Smoothed time profiles of the emission measure $EM(t)$ (black in left panels) and the electron temperature $T_e(t)$ (red in left panels, and phase diagram $T_e(EM)$ (right panels) of three loop episodes observed in an active region with AIA/SDO. A moving average background has been subtracted in all time profiles, and the amplitudes are normalized by their standard deviation from the means. A quasi-stationary time interval with near-elliptical phase trajectories is colored with red. The quasi-periodicity and the phase delay indicate a limit-cycle behavior of the evaporation-condensation cycle in solar flares (Froment et al. 2015)

Periodically repeating heating-condensation cycles were found to be coupled with transverse kink-mode oscillations in some active region loops (Kohutova and Verwichte 2016, 2017a,b; Verwichte and Kohutova 2017; Verwichte et al. 2017), see Fig. 9.10.

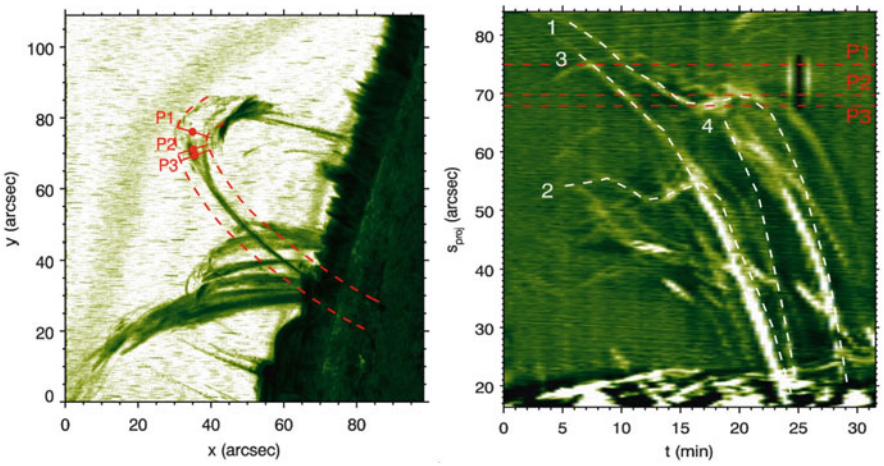

Fig. 9.10 Observations of coronal rain in an oscillating loop: *Left:* Hinode/SOT Ca II H band observations on 2012-04-16, 15:04 UT; *Right:* Time-slice plot with time on x-axis and altitude on y-axis (Verwichte et al. 2017)

9.7 Coronal Loops: Heating Function

The heating function term $E_h(s,t)$ in the hydrodynamic energy equation has (a generally unknown) time and spatial dependence. In 1-D hydrodynamic flux tube models (with loop length coordinate s), which is often approximated assuming an adiabatic state, the energy balance is given by (e.g., Rosner et al. 1978),

$$E_h(s,t) - E_c(s,t) - E_r(s,t) = 0\,. \tag{9.7.1}$$

Here E_h is the volumetric heating rate, E_c is the conductive energy loss rate, and E_r is the radiative energy loss rate. The three most common spatial heating functions of loops are the uniform, footpoint, and apex heating functions. The spatial shape of the nonuniform heating function is generally parameterized with an exponential function (e.g., Serio et al. 1981), and the time dependence has been approximated with a Gaussian function,

$$E_H(s,t) = H_0 \, \exp\left(-\frac{(t-t_m)^2}{2\tau_{heat}^2}\right) \exp\left(-\frac{s}{s_H}\right) \begin{cases} s_H > 0 & \text{for footpoint heating} \\ s_H = \infty & \text{for uniform heating} \\ s_H < 0 & \text{for apex heating} \end{cases} \tag{9.7.2}$$

were t_m is the time of maximum heating, τ_{heat} the gaussian width of the heating time interval, s_H is the heating scale height, and H_0 is the volumetric heating rate at the footpoint.

One obvious case we can rule out at this stage is the uniform heating function (constant in space and time), because it would not be able to explain the observed over-density of cool loops in EUV (Lenz et al. 1999; Aschwanden et al. 1999, 2000). None of the heating function approximations fits the observed density profiles derived from DEM forward-fitting or inversions, which created a new conundrum that violated previous steady-state models. Besides the over-density with respect to the RTV steady-state solution, EUV loops were found to reveal super-hydrostatic scale heights and exceptionally flat temperature profiles. These critical loop properties led to the diagnostic decision tree as shown in Fig. 9.11. The ratio of the radiative to the conductive cooling time,

$$\left(\frac{\tau_{rad}}{\tau_{cond}}\right) \approx \frac{T^4}{n_e^2 L^2} \tag{9.7.3}$$

was found to vary over orders of magnitude for cool and hot coronal loops (Fig. 9.12), but can be reproduced with simulations of impulsively heated loop strands (Klimchuk 2006, 2009).

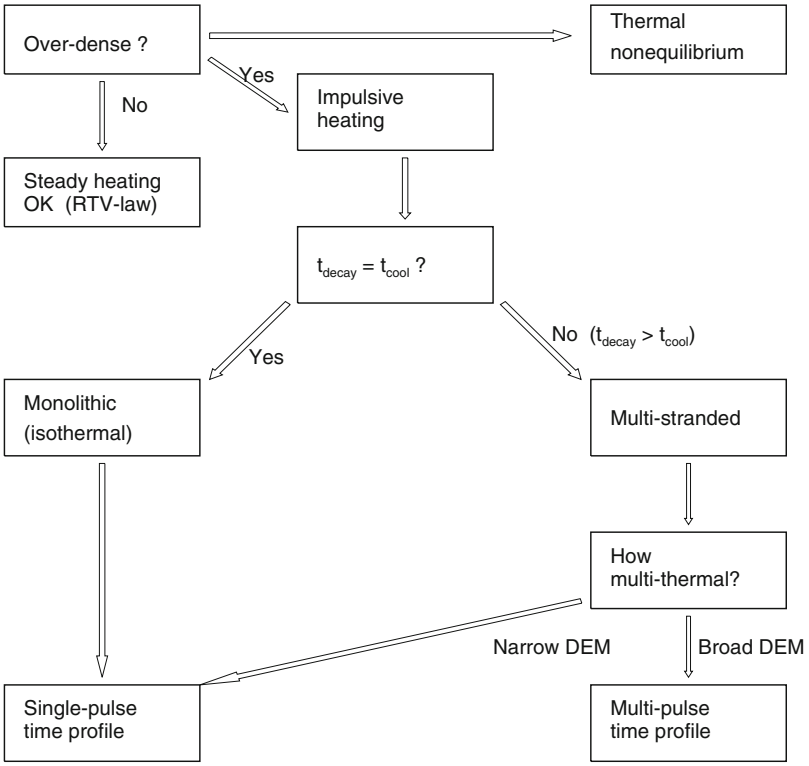

Fig. 9.11 Flow chart of the diagnostics of coronal loop heating scenarios, starting from the observed electron density, the observed decay time (compared with the theoretical cooling time), and the temperature widths of the DEMs (adapted from Klimchuk 2009)

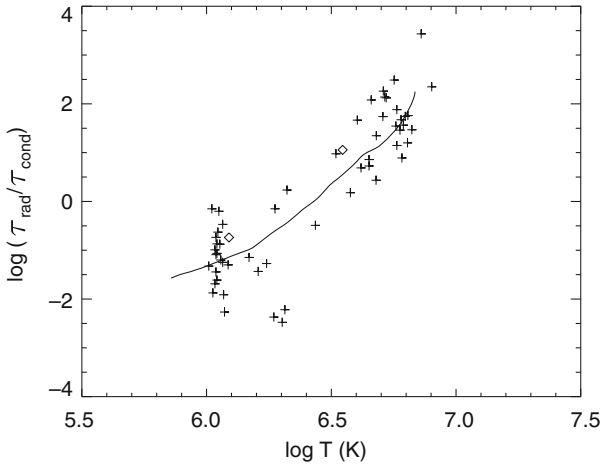

Fig. 9.12 Ratio of radiative to conductive cooling times versus temperature of loops observed with TRACE and SXT/Yohkoh (crosses). The solid curve is the cooling track of an impulsively heated loop strand simulation (Klimchuk 2006, 2009)

Another case that is unlikely is the loop apex heating scenario. Although a statistical temperature increase is generally observed in the corona above the limb, which has been interpreted in terms of a temperature profile of a single loop that is heated from the top (Reale 2002), this temperature gradient is more naturally explained in terms of the hydrostatic weighting bias in an inhomogeneous solar corona (Aschwanden and Nitta 2000). Consequently, only the case of footpoint heating survives as a realistic spatial heating function of coronal loops.

For the temporal dependence, delta-functions, rectangular, triangular, or Gaussian functions have been employed. Fortunately we have additional constraints that restrict the time-dependence of the heating function in loops, namely the observed life time (or decay time) of a loop, which has to match the cooling time as obtained in hydrodynamic simulations. However, hydrodynamic simulations of the time evolution of coronal loops exhibited that the simulated life times of loops were found to be always shorter than the observed life times (Warren et al. 2002, 2003), which led to the conclusion that a sequence of subsequentially (overlapping and superimposed) heating episodes only can explain the observed time evolution of active region loops (Fig. 9.6), so that an active region loop consists of a collection of small-scale strands (or filaments) that are impulsively heated and are cooling through the EUV passbands (Warren et al. 2002, 2003; Winebarger et al. 2003; Mulu-Moore et al. 2011). While the decay time discrepancy is based on multi-stranded loops observed with TRACE, it has not been tested yet whether monolithic loops with finer widths exhibit the same decay time discrepancy, such as the finest loops discovered in Hi-C data down to $w \approx 100$–500 km (Peter et al. 2013; Brooks et al. 2013; Aschwanden and Peter 2017; see Figs. 9.4 and 9.5). Multi-stranded hydrodynamic models have also difficulty to reproduce the diffuse hot plasma in an

active region (Warren et al. 2010a). On the other side, steady-state heating was found to be consistent with hot loops observed with XRT in the core of active regions, as well as with *"moss"* structures at the footpoint of high-temperature loops (Warren et al. 2010b).

Special cases of the heating function have been simulated: the *explosive heating* scenario with very fast heating to high temperatures, which leads to near-saturated thermal conduction (Bradshaw and Cargill 2006, 2013); simulations with nonuniform loop cross-section areas, nonuniform heating, asymmetric loop shapes, and asymmetric heating (Mikic et al. 2013); periodic and overlapping heating pulses that mimic quasi-steady heating (Testa et al. 2005); heating pulses in a multi-stranded system randomly distributed in time (Patsourakos and Klimchuk 2006; Guarrasi et al. 2010); or turbulent heating rates (Chae et al. 2002).

9.8 Coronal Loops: The 0-D EBTEL Code

The hydrodynamics of the solar corona is generally simplified in terms of one-dimensional (1-D) flux tubes that represent rigid conduits for plasma flows, since the plasma-β parameter is less than unity in most coronal regions, which implies that the magnetic pressure exceeds the thermal pressure and thus forms impenetrable flux tubes without cross-field transport. The reduction of the coronal hydrodynamics to a 1-D problem can further be simplified to a 0-D problem, since thermal conduction and flows tend to smooth out plasma gradients along the magnetic field. An efficient 0-D hydrodynamic code, called the *"enthalpy-based thermal evolution of loops" (EBTEL)* code has been developed that approximately describes the evolution of the average temperature, pressure, density, and differential emission measure (DEM) distribution inside a coronal loop strand, where the enthalpy plays a major role in the energy budget (Klimchuk et al. 2008; Cargill et al. 2012a,b). The motivation for creating such an efficient hydrodynamic code came from the desire to model coronal loops as a superposition of thousands of (observationally unresolved) miniature loops, also called *"elemental loop strands"*, as they are invoked in nanoflare heating models.

We outline the derivation of the 0-D hydrodynamic EBTEL model according to Klimchuk et al. (2008). The 1-D time-dependent hydrodynamic equation for energy conservation is,

$$\frac{\partial E}{\partial t} = -\frac{\partial}{\partial s}(Ev) - \frac{\partial}{\partial s}(Pv) - \frac{\partial F_c}{\partial s} + Q - n^2\Lambda(T) + \rho g_{\parallel} v \,, \tag{9.8.1}$$

where E is the combined thermal and kinetic energy density (defined as $E = P/(\gamma - 1)$ in terms of the adiabatic index γ in Cargill et al. 2012a),

$$E = \frac{3}{2}P + \frac{1}{2}\rho v^2 \,, \tag{9.8.2}$$

s is the spatial coordinate along the magnetic field, n is the electron number density, T is the electron temperature, P is the total pressure, v is the bulk velocity, F_c is the conductive heat flux, Q is the volumetric heating rate (equivalent to $E_H(s,t)$ in Sect. 9.7), $g_\parallel$ is the gravity component along the magnetic field, and $\Lambda(T)$ is the optically thin radiative loss function. The usual assumptions of 1-D hydrodynamic codes are applied, such as symmetric loops and constant loop cross-sections, which are still a matter of debate. Furthermore, neglecting the kinetic energy (assuming subsonic flows) and gravity terms (for loops shorter than the gravitational scale height), we obtain,

$$\frac{3}{2}\frac{\partial P}{\partial t} \approx -\frac{5}{2}\frac{\partial}{\partial s}(Pv) - \frac{\partial F_c}{\partial s} + Q - n^2\Lambda(T) \; . \tag{9.8.3}$$

Integrating Eq. (9.8.3) over the loop length L and applying a vanishing velocity and heat flux at the apex due to the loop symmetry, we obtain,

$$\frac{3}{2}L\frac{\partial\langle P\rangle}{\partial t} \approx \frac{5}{2}(P_0 v_0) + F_0 + L\langle Q\rangle - R_c \; , \tag{9.8.4}$$

where L is the coronal loop half length, the quantities $\langle P\rangle$ and $\langle Q\rangle$ indicate spatial averages along the coronal loop section, P_0 is the pressure and v_0 is the velocity at the footpoint of the loop (at the base of the corona), $(5/2)P_0v_0$ is the enthalpy flux, F_0 is the heat flux, and $R_c \approx \langle n^2\rangle\Lambda(\langle T\rangle)L$ is the radiative cooling rate per unit cross-sectional area in the corona. A similar averaging can be applied to the transition region,

$$\frac{3}{2}l\frac{\partial\langle P_{tr}\rangle}{\partial t} \approx \frac{5}{2}(P_0 v_0) + F_0 + l\langle Q_{tr}\rangle - R_{tr} \; , \tag{9.8.5}$$

where l is the length from the coronal base to the apex, and R_{tr} is the radiative cooling rate in the transition region. Assuming that the enthalpy flux is proportional to the temperature, therefore being much smaller at the top of the chromosphere than in the corona, i.e., $l \ll L$, it can be ignored in Eq. (9.8.5), leading to,

$$\frac{5}{2}(P_0 v_0) \approx -F_0 - R_{tr} \; . \tag{9.8.6}$$

In static equilibrium, the heat flux and radiative power is balanced, i.e., $|F_0| = R_{tr}$, which yields with Eqs. (9.8.4) and (9.8.6),

$$\frac{\partial\langle P\rangle}{\partial t} \approx \frac{2}{3}\left[\langle Q\rangle - \frac{1}{L}(R_c + T_{tr})\right] \; . \tag{9.8.7}$$

This equation reflects the energetics of the combined corona and transition region system, with a source term $\langle Q\rangle$ and loss term $(R_c + R_{tr})/L$.

After we quantified the pressure evolution $\partial\langle P\rangle/\partial t$ we want to derive the density evolution $\partial\langle n\rangle/\partial t$, which is obtained by setting the time derivative of the electron

column density $\langle n \rangle L$ equal to the flux of electrons through the coronal base, i.e., $\partial(\langle n \rangle L)/\partial t = J_0 \approx nv$, and using the ideal gas law $P = 2k_B nT$,

$$\frac{\partial \langle n \rangle}{\partial t} = \frac{c_2}{5c_3 k_B L \langle T \rangle}(F_0 + R_{tr}) \ , \tag{9.8.8}$$

where the constants refer to the temperature ratios $c_2 = \langle T \rangle / T_a$ and $c_3 = T_0/T_a$, T_a being the apex temperature, and T_0 the coronal base temperature. The classical expression for the heat flux is

$$F_0 = -\kappa_0 T^{5/2} \frac{\partial T}{\partial s} \approx -\frac{2}{7}\kappa_0 \frac{T_a^{7/2}}{L} \ . \tag{9.8.9}$$

Combining then Eqs. (9.8.7) and (9.8.8) with the ideal gas law leads then to the temperature evolution $\partial \langle T \rangle / \partial t$,

$$\frac{\partial \langle T \rangle}{\partial t} \approx \langle T \rangle \left(\frac{1}{\langle P \rangle} \frac{\partial \langle P \rangle}{\partial t} - \frac{1}{\langle n \rangle} \frac{\partial \langle n \rangle}{\partial t} \right) \ , \tag{9.8.10}$$

Similarly, the plasma velocity at the base of the corona can be obtained from the electron flux J_0,

$$v_0 = \frac{c_3}{c_2} \frac{2k_B \langle T \rangle J_0}{\langle P \rangle} \ . \tag{9.8.11}$$

The numerical EBTEL code uses the three evolutionary equations for the pressure (Eq. 9.8.7), the density (Eq. 9.8.8), and the temperature (Eq. 9.8.10) to calculate the time evolutions $P(t)$, $n(t)$, $T(t)$ in incremental time steps, starting from some initial conditions at time $t = 0$. An example of such a time-dependent 0-D solution is shown in Fig. 9.13, which is compared with a classical 1-D hydrodynamic solution using the *Adaptive Refined Godunov Solver (ARGOS)* code (Antiochos et al. 1999), demonstrating an agreement within $\approx 20\%$ in most time steps. The EBTEL code contains some variable parameters that can be adjusted based on 1-D hydrodynamic simulations, such as $c_1 = R_{tr}/R_c = 4.0$, $c_2 = \langle T \rangle / T_a = 0.87$, and $c_3 = T_0/T_a = 0.5$. Modifications of the EBTEL code include the energy flux and particle flux of nonthermal electron beams (Klimchuk et al. 2008). Generally, the differential emission measure (DEM) distributions computed with the EBTEL code, using the scenario of strong evaporation (by thermal conduction only) and strong condensation (when the heat flux is much less than the radiative losses), are not valid when nonthermal particles are important, such as in the case of beam-driven evaporation during solar flares. A key advantage of the 0-D EBTEL code is that it requires about four orders of magnitude less computation time than traditional 1-D hydrodynamic codes (such as ARGOS).

Improvements of the EBTEL model include gravitational stratification, a physically motivated treatment of radiative cooling (Cargill et al. 2012a), and nonequilibrium ionization (Bradshaw and Klimchuk 2011). Comparisons of the EBTEL code

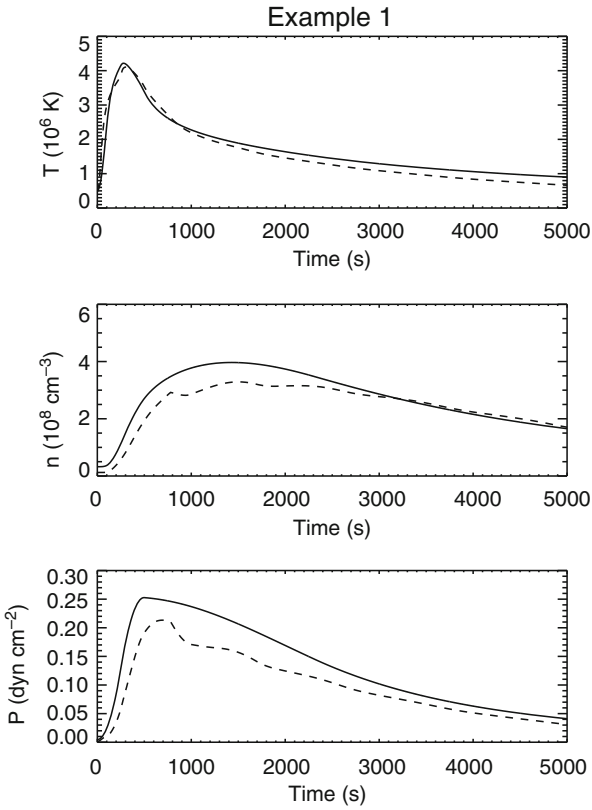

Fig. 9.13 Evolution of the coronal-averaged temperature (top), electron density (middle), and pressure (bottom), for a loop strand heated impulsively over a duration of 500 s. The solid curves are computed with the 0-D EBTEL code, while the dashed curves are computed with the 1-D ARGOS code. Classical heat flux is assumed (Klimchuk et al. 2008)

with other 0-D hydrodynamic models (Kuin and Martens 1982; Kopp and Poletto 1993; Cargill 1994; Fisher and Hawley 1990; Aschwanden and Tsiklauri 2009) have been conducted in Cargill et al. (2012b). Applications of the EBTEL code to solar flare data involves EIS/Hinode and AIA/SDO observations (e.g., Raftery et al. 2009; Ugarte-Urra and Warren 2014; Viall and Klimchuk 2012).

9.9 Coronal Loops: 1-D Hydrodynamics

1-D hydrodynamic codes have been the work horse for modeling of coronal loops or prominences for several decades. The one-dimensionality is a natural consequence of the fact that coronal plasma can only follow the magnetic field lines in the low plasma-β corona. All parameters in 1-D flux tubes have a dependence on the 1-

D spatial coordinate s, as well as on the time t, such as the electron temperature $T(s,t)$, the electron density $n(s,t)$ or mass density $\rho(s,t) = m_p n(s,t)$, the velocity $v(s,t)$, the heating rate $Q(s,t)$, the conductive flux $F_c(s,t)$, the pressure $P(s,t)$, the internal energy $E(s,t) = (3/2)P(s,t) + (1/2)\rho(s,t)v^2(s,t)$, and the radiative loss rate $E_r(s,t) = n^2(s,t)\Lambda(T(s,t))$. A hydrodynamic code, such as the ARGOS code (Antiochos et al. 1999), solves the time evolution of these parameters from the transport equations for mass, momentum, and energy in a 1-D plasma,

$$\frac{\partial}{\partial t}\rho + \frac{\partial}{\partial s}(\rho v) = 0 \,, \tag{9.9.1}$$

$$\frac{\partial}{\partial t}(\rho v) + \frac{\partial}{\partial s}(P + \rho v^2) = -\rho g_{\parallel} \,, \tag{9.9.2}$$

$$\frac{\partial E}{\partial t} = -\frac{\partial}{\partial s}(Ev) - \frac{\partial}{\partial s}(Pv) - \frac{\partial F_c}{\partial s} + Q - n^2\Lambda(T) + \rho g_{\parallel} v \,, \tag{9.9.3}$$

where the conductive flux F_c is,

$$F_C(s) = \left[-\kappa T^{5/2}(s)\frac{dT(s)}{ds}\right] = -\frac{2}{7}\kappa\frac{d}{ds}\left[T^{7/2}(s)\right] \,, \tag{9.9.4}$$

with $\kappa = 9.2 \times 10^{-7}$ (erg s^{-1} cm^{-1} K$^{-7/2}$) the classical Spitzer conductivity. The least known parameter is the spatio-temporal heating function $Q(s,t)$, for which various parameterizations have been used to mimic uniform, footpoint, or apex heating (Sect. 9.7). There exist also various parameterizations of the radiative loss function $\Lambda(T)$, usually approximated by piece-wise power law functions. While numerical codes have been designed to solve the coupled equation system of Eqs. (9.9.1–9.9.4), attempts have been made to simplify the analytical function that approximates the radiative loss function (e.g., Landini and Landi 2002; Dudik et al. 2009; Martens 2010; Bradshaw 2008), to specify various shapes of the spatial heating function (Serio et al. 1981), to quantify analytical approximations of the numerical solutions (Aschwanden and Tsiklauri 2009), or to include nonequilibrium ionization (e.g., Bradshaw and Mason 2003, Bradshaw 2008).

The radiative loss function $\Lambda(T)$ is generally approximated with piece-wise power law functions, following the initial characterization by Rosner et al. (1978). An alternative form is used by Landini and Landi (2002),

$$E_r = -n^2\Lambda(T) = -C\frac{p_0^2}{T^{2.5}} \,, \tag{9.9.5}$$

with $C \approx 2 \times 10^{12}$ K$^{5/2}$ cm^3 s^{-1} erg^{-1}, based on radiative loss calculations in an optically thin plasma using the Arcetri Spectral Code in the 10^4–10^8 K temperature range (Landi and Landini 1999). Similarly, Martens (2010) characterizes the radiative loss function with a power law function

$$E_r = -n^2\Lambda(T) = -\chi_0\, p_0^2\, T^{-(2+\gamma)} \,, \tag{9.9.6}$$

where $\chi_0 = 10^{12.41}$ is in cgs-units, while the heating function is rendered with a similar power law relation,

$$Q = Q_0 \, p_0^{\beta} \, T^{\alpha} \, . \tag{9.9.7}$$

This parameterization makes the energy equation (Eq. 9.9.3) integrable and an analytical solution is obtained for the hydrostatic temperature profile $T(s)$ and the RTV-type scaling law $P_0 L \propto T_{max}^3$, for a selection of heating functions $Q(s)$, as well as for a loop cross-section that is expanding with height (Martens 2010). A similar power law approach is used in analytical models of static coronal loops by Dudik et al. (2009), namely

$$E_r = -n^2 \Lambda(T) = -\chi_0 \, n_e^2 \, T^{-\sigma} \, , \tag{9.9.8}$$

with a coefficient of $\sigma = -1/2$ (Kuin and Martens 1982). In numerical models one can also interpolate the values calculated with an atomic data base, e.g., CHIANTI (see Sect. 2.3).

An analytical approximation of the temperature profile $T(s)$ can be obtained by neglecting the radiative loss during the initial heating phase (Aschwanden and Tsiklauri 2009), so that the heating rate $Q(s)$ essentially balances the conductive loss rate $\nabla F_c(s)$, which yields a differential equation of second order in the spatial coordinate s,

$$E_H(s) = \frac{d}{ds}\left[-\kappa T^{5/2}(s) \frac{dT(s)}{ds}\right] = -\frac{2}{7}\kappa \frac{d^2 T(s)^{7/2}}{ds^2} \, . \tag{9.9.9}$$

This second-order differential equation can be turned into an double-integral equation by expressing it as an explicit function of $T(s)$,

$$T(s) = \left[\int ds \int -\frac{7}{2\kappa} E_H(s) \, ds\right]^{2/7} \, . \tag{9.9.10}$$

which yields the following solution for the case of uniform heating,

$$T^{uni}(s) = T_2 \left[\left(\frac{s}{L}\right)\left(2 - \frac{s}{L}\right)\right]^{2/7} \, . \tag{9.9.11}$$

The evolution of the electron density $n(t)$ in the loop can be understood in terms of the *Neupert effect*, which in essence states that the accumulated density in a heated loop is an integral function of the heating rate, because the chromospheric evaporation rate into the coronal loop is a function of the chromospheric heating rate or energy input. If we neglect cooling during the heating phase, free energy is continuously added to the loop in form of evaporating material, which increases the density in the loop monotonously, peaking at the end of the heating phase. Parameterizing the heating function $Q(t)$ with a Gaussian function yields a Gaussian

temperature profile $T(t) \propto Q(t)$, while the density function follows the integral of the Gaussian function, $n(t) \propto \int Q(t)ds$, which predicts a maximum of the density function $n(t)$ at approximately the half decay time of the heating function, as sketched in Fig. 9.14. The analytical approximations of the temperature $T(t)$ and density profiles $n(t)$ have been found to agree well with numerical hydrodynamic simulations (Aschwanden and Tsiklauri 2009), as shown in Fig. 9.14. A typical characteristic of the temperature-density phase diagram (Fig. 9.14, right panel) is the hysteresis curve of the density peak lagging behind the temperature peak, following the *Jakimiec power law relationship*,

$$\frac{T(t)}{T_p} \approx \left(\frac{n(t)}{n_p}\right)^2 , \tag{9.9.12}$$

which was found to scale approximately with a power law slope of ≈ 2, as found in many earlier hydrodynamic simulations (e.g., Jakimiec et al. 1992; Serio et al. 1981; Sylwester et al. 1993).

While most hydrodynamic simulations of coronal loops assume ionization equilibrium, this assumption has been scrutinized by solving the detailed ionization

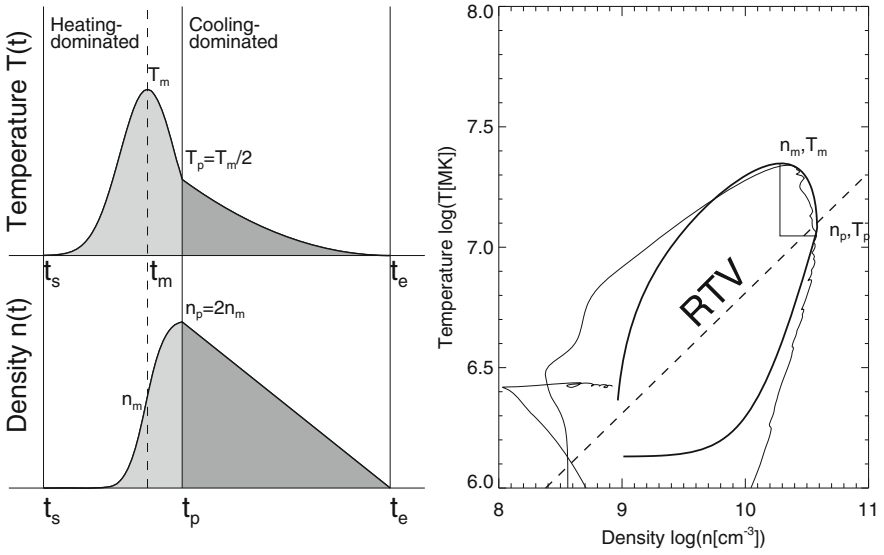

Fig. 9.14 Hydrodynamic time evolution of the electron temperature $T(t)$ and density $n_e(t)$ of a simulation of an impulsively-heated flare loop (see Aschwanden and Tsiklauri 2009), shown as time profiles (left panel) and as an evolutionary phase diagram $T_e(n_e)$ (right panel). The evolution of the hydrodynamic simulation is shown as exact numerical solution (curve with thin linestyle in right panel), and as an analytical approximation (curves with thick linestyle in both panels), along with the prediction $T_e \propto n_e^{1/2}$ of the RTV scaling law for uniform steady heating (dashed line in right panel) (Aschwanden and Shimizu 2013)

balance equation for each ion of the fifteen most abundant elements of the solar atmosphere for the case of a cooling loop (Bradshaw and Mason 2003). The ionization balance equation for each ion is,

$$\frac{\partial Y_i}{\partial t} + \frac{\partial}{\partial s}(Y_i v) = n(I_{i-1}Y_{i-1} + R_i Y_{i+1} - I_i Y_i - R_{i-1}Y_i) \,, \tag{9.9.13}$$

where Y_i denotes the fractional population of ion level i of element Y, the coefficients I_i and R_i are the ionization and recombination rates from/to ion level i, n is the electron number density, t is the time, and s is the spatial location along the loop. Significant deviations from equilibrium are found in the coronal and footpoint regions of the loop, especially in low-density coronal regions that cause the recombination rate to be rarer. For another case of a loop subjected to transient heating near the apex, an up to 5 times lower plasma emissivity is found in equilibrium compared with nonequilibrium emissivity, almost entirely due to the response of the coronal Fe ions (Bradshaw and Mason 2003).

9.10 Coronal Loops: Magnetic Modeling

Some new developments of magnetic field modeling in active regions are described in Sect. 8.1. It was realized that none of the magnetic field extrapolation methods warrants that the theoretically calculated field lines match the the observed geometry of coronal loops, as observed in EUV or in soft X-rays. Since the plasma β-parameter in the solar corona is generally less than unity, coronal loops visible in EUV or soft X-rays are supposed to trace the coronal magnetic field. There are two new strategies that take the observed loop geometry into account: (i) stereoscopic triangulation (which became feasible with the STEREO mission), and (ii) automated loop tracing in EUV and soft X-ray images, which both provide stringent constraints for 3-D modeling of the coronal magnetic field.

Since it was recognized that the photosphere and lower chromosphere are generally not force-free (Metcalf et al. 1995), the force-free extrapolation of coronal magnetic field lines from a non-force-free lower boundary, which is the *modus vivendi* for *non-linear force-free field (NLFFF)* codes using photospheric magnetograms (or vector data), the accuracy of NLFFF codes became questionable. A refinement of the NLFFF optimization method was proposed by introducing a weighting function that minimizes the force balance between the non-force-free photosphere and the force-free lower boundary of the computation box, which is a magneto-hydrostatic approach (Wiegelmann 2004). Well-posed boundaries are studied in Amari et al. (2006). A method of preprocessing was developed which drives the observed non-force-free data towards suitable boundary conditions for force-free extrapolation codes, minimizing the force balance and the torque-free condition (Wiegelmann et al. 2006; Metcalf et al. 2008; Wiegelmann et al. 2012). A benchmark test of 9 different NLFFF codes (including optimization,

magneto-frictional, Grad-Rubin based, and Green's function-based methods) has been arranged in Schrijver et al. (2006), which demonstrated that the agreement is always best in the lower central region of the volume, where the field and electrical currents are strongest and the effects of boundary conditions weakest, while the solutions in the outer domains show a high sensitivity on the specific boundary conditions. The fastest-converging and best-performing model for these analytical test cases turned out to be the Wheatland et al. (2000) optimization algorithm, as implemented by Wiegelmann (2004). A similar benchmark test with 6 different NLFFF codes was carried out by Metcalf et al. (2008), revealing differences in the free energy by about a factor of 2 for the different codes. The non-force-free boundary problem, however, can be circumvented with force-free codes that fit coronal loop features, rather than photospheric data, for instance with stereoscopic loop detection codes (Aschwanden 2013a), or with automated loop tracing codes (Aschwanden et al. 2014). The most comprehensive benchmark test of 12 NLFFF codes was carried out by De Rosa et al. (2009), using Hinode/SOT-SP, Hinode/XRT, EUV/STEREO, and MDI/SOHO observations. The following critical requirements for successful NLFFF modeling were assessed: (i) sufficiently large areas of vector magnetic field data are needed, (ii) the uncertainties in the boundary data need to be incorporated in the NLFFF algorithms, and (iii) a more realistic physical model is needed to approximate the photosphere-to-corona interface (De Rosa et al. 2009). It was shown that the incorporation of measurement errors implemented into the various NLFFF codes significantly improves the quality of NLFFF solutions from imperfect boundary conditions (Wiegelmann and Inhester 2010; Wiegelmann et al. 2012).

Using various methods of potential field methods (potential field source surface (PFSS), unipolar charges, dipolar models) and non-potential force-free field methods (NLFFF), it was shown that all these theoretical magnetic field models exhibit a misalignment of order $\approx 20°$–$40°$ with respect to the observed loop directions measured in EUVI/STEREO images, compared either with their 2-D projections, or with the 3-D coordinates as triangulated from stereoscopic observations (Sandman et al. 2009; Aschwanden and Sandman 2010; Sandman and Aschwanden 2011). A residual misalignment of $\approx 11°$–$17°$ has been attributed to the non-potentiality of active regions (Aschwanden and Sandman 2010).

Newly developed NLFFF codes include: a magneto-hydrostatic approach (Flyer et al. 2004); a Grad-Rubin method based on partial derivatives instead of finite differences (Song et al. 2006); NLFFF codes in spherical geometry instead of Cartesian geometry (Wiegelmann 2007); the so-called flux insertion method based on the geometry of observed Hα filaments (Van Ballegooijen 2004; Van Ballegooijen et al. 2007; Bobra et al. 2008; Titov et al. 2014); the vertical current approximation VCA-NLFFF code (Aschwanden 2013b,c, 2016; Aschwanden and Malanushenko 2013); and a stereoscopic triangulation code using automatically traced coronal loops (Aschwanden et al. 2014). An example of a VCA-NLFFF solution with automatically traced loops is shown in Fig. 9.15.

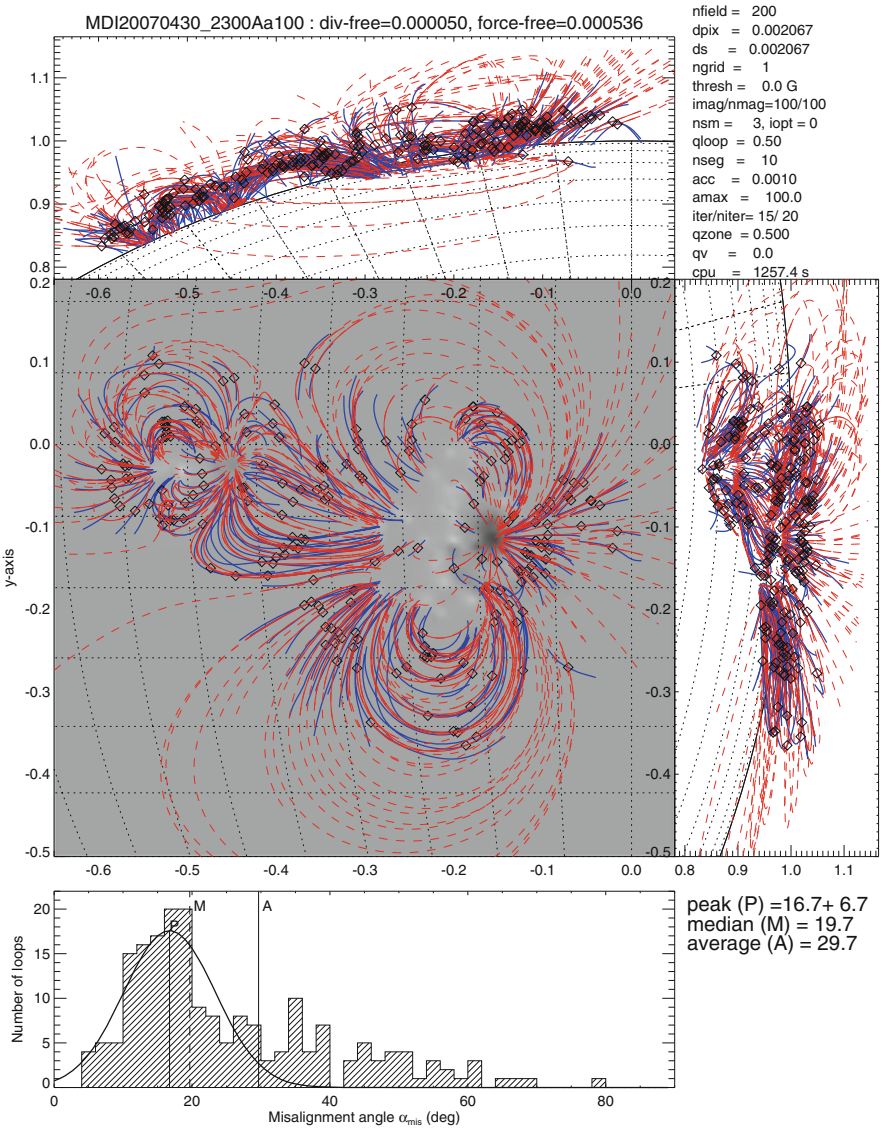

Fig. 9.15 Active region NOAA 10953, observed on 2007 April 30, 23:00 UT: Stereoscopically triangulated loops observed with EUVI/STEREO (blue curves) are compared with a solution of the VCA-NLFFF code (red curves), overlaid on a MDI/SOHO magnetogram. The upper 3 panels represent orthogonal views, and the histogram (bottom) shows the distribution of 3-D misalignment angles, with an average of $\mu_3 = 16.7^\circ \pm 6.7^\circ$ (Aschwanden et al. 2012)

References

(9.1) Coronal Loops: Stereoscopy and 3-D Geometry

Aschwanden, M.J., Newmark, J.S., Delaboudiniere, J.P., et al. 1999, *3-D stereoscopic analysis of solar active region loops. I. SOHO/EIT observations at temperatures of (1.0–1.5)* $\times 10^6$ *K*, ApJ 515, 842, [218 c, 12 c/y].

Aschwanden, M.J., Alexander, D., Hurlburt, N., et al. 2000, *3-D stereoscopic analysis of solar active region loops. II. SOHO/EIT observations at temperatures of 1.5–2.5 MK*, ApJ 531, 1129, [88 c, 5 c/y].

Aschwanden, M.J., Wülser,J.P., Nitta,N., et al. 2008, *First 3-D reconstruction of coronal loops with the STEREO A and B spacecraft. I. Geometry*, ApJ 679, 827, [78 c, 8 c/y].

Aschwanden, M.J. 2009, *The 3-D geometry, motion, and hydrodynamic aspects of oscillating coronal loops*, SSRv 149, 31, [40 c, 5 c/y].

Aschwanden, M.J., Wülser, J.P., Nitta, N., et al. 2012, *Solar stereoscopy with STEREO /EUVI A and B spacecraft from small (6°) to large (170°) spacecraft separation angles*, SoPh 281, 101, [6 c, 2 c/y].

Aschwanden, M.J. 2013, *A nonlinear force-free magnetic field approximation suitable for fast forward-fitting to coronal loops. I. Theory*, SoPh 287, 323, [17 c, 4 c/y].

Feng, L., Inhester, B., Solanki, S.K., et al. 2007, *First stereoscopic coronal loop reconstruction from STEREO SECCHI images*, ApJ 671, L205, [53 c, 5 c/y].

Gary, G.A. 1997, *Rendering 3-D solar coronal structures*, SoPh 174, 241, [15 c, 0.7 c/y].

Gary, G.A. and Alexander, D. 1999, *Constructing the coronal magnetic field by correlating parameterized magnetic field lines with observed coronal plasma structures*, SoPh 186, 123, [35 c, 2 c/y].

Lundquist, L.L, Fisher, G.H., and McTiernan, J.M. 2008, *Forward modeling of active region coronal emissions. I. Methods and testing*. ApJSS 179, 533, [26 c, 3 c/y].

Sandman, A.W. and Aschwanden, M.J. 2011, *A new method for modeling the coronal magnetic field with STEREO and submerged dipoles*, SoPh 270, 503, [17 c, 3 c/y].

Schrijver, C.J., Sandman, A.W., Aschwanden, M.J., et al. 2004, *The coronal heating mechanism as identified by full-Sun visualizations*, ApJ 615, 512, [97 c, 7 c/y].

Wiegelmann, T., and Neukirch, T. 2002, *Including stereoscopic information in the reconstruction of coronal magnetic fields*, SoPh 208, 233, [46 c, 3 c/y].

(9.2) Coronal Loops: Cross-Sectional Widths

Abramenko, V.I., Yurchyshyn, V.B., Goode, P.R., et al. 2012, *Detection of small-scale structures in the Quiet Sun with the New Solar Telescope (NST)*, ApJ 756, L27, [18 c, 3 c/y].

Alexander, C.E., Walsh, R.W., Régnier, S., et al. 2013, *Anti-parallel EUV flows observed along active region filament threads with Hi-C*, ApJ 775, L32, [24 c, 5 c/y].

Antolin, P., Vissers, G., Pereira, T.M.D., et al. 2015, *The multithermal and multi-stranded nature of coronal rain*, ApJ 806, 81, [34 c, 14 c/y].

Antolin, P. and Rouppe van der Voort, L. 2012, *Observing the fine structure of loops through high-resolution spectroscopic observations of coronal rain with the CRISP instrument at the Swedish Solar Telescope*. ApJ 745, 152, [80 c, 15 c/y].

Aschwanden, M.J. and Wülser, J.P. 2011, *3-D reconstruction of active regions with STEREO*, JASTP 73, 1082, [7 c, 1 c/y].

Aschwanden, M.J. and Boerner, P. 2011, *Solar corona loop studies with the AIA. I. Cross-temperature structure* ApJ 732, 81, [79 c, 12 c/y].

Aschwanden, M.J. and Schrijver, C.J. 2011, *Coronal loop oscillations observed with AIA. Kink mode with cross-sectional and density oscillations*, ApJ 736, 102, [88 c, 14 c/y].

Aschwanden, M.J., Boerner, P., Schrijver, C.J., et al. 2013, *Automated temperature and emission measure analysis of coronal loops and active regions observed with the AIA on the SDO*, SoPh 283, 5, [78 c, 17 c/y].

Aschwanden, M.J. and Peter, H. 2017, *The width distribution of loops and strands in the solar corona. - Are we hitting rock bottom*, ApJ 840, 4, [7 c, 7 c/y].

Brooks, D.H., Warren, H.P., and Ugarte-Urra, I. 2012, *Solar coronal loops resolved by Hinode and the SDO*. ApJ 755, L33, [50 c, 9 c/y].

Brooks, D.H., Warren, H.P., Ugarte-Urra, I., et al. 2013, *High spatial resolution observations of loops in the solar corona*, ApJ 772, L19, [47 c, 10 c/y].

Brooks, D.H., Reep, J.W., and Warren, H.P. 2016, *Properties and modeling of unresolved fine structure loops observed in the solar transition region by IRIS*, ApJ 826, L18, [4 c, 3 c/y].

Morton, R.J. and McLaughlin, J.A. 2013, *Hi-C and AIA observations of transverse MHD waves in active regions*, A&A 556, C1.

Mulu-Moore, F.M., Winebarger, A.R., Warren, H.P., et al. 2011, *Determining the structure of solar coronal loops using their evolution*, ApJ 733, 59, [23 c, 4 c/y].

Peter, H., Bingert, S., Klimchuk, J.A., et al. 2013, *Structure of solar coronal loops: From miniature to large-scale*, A&A 556, A104, [52 c, 12 c/y].

Winebarger, A.R., Walsh, R.W., Moore, R., et al. 2013, *Detecting nanoflare heating events in subarcsecond inter-moss loops using Hi-C*, ApJ 771, 21, [32 c, 7 c/y].

Winebarger, A.R., Cirtain, J., Golub, L., et al. 2014, *Discovery of finely structured dynamics solar corona observed in the Hi-C Telescope*, ApJ 787, L10, [11 c, 3 c/y].

Tiwari, S.K., Moore, R.L., Winebarger, A.R., et al. 2016, *Transition-region/coronal signatures of magnetic setting of sunspot penumbral jets: Hinode (SOT/FG), Hi-C, and SDO/AIA observations*, ApJ 816, 92, [9 c, 6 c/y].

(9.3) Coronal Loops: Multi-Strand Structure

Antolin, P., Vissers, G., Pereira, T.M.D., et al. 2015, *The multithermal and multi-stranded nature of coronal rain*, ApJ 806, 81, [34 c, 14 c/y].

Aschwanden, M.J. and Nightingale, R.W. 2005, *Elementary loop structures in the solar corona analyzed from TRACE triple-filter images*, ApJ 633, 499, [108 c, 9 c/y].

Aschwanden, M.J., Nightingale, R.W., and Boerner, P. 2007, *A statistical model of the inhomogeneous corona constrained by triple-filter measurements of elementary loop strands with TRACE*, ApJ 656, 577, [26 c, 2 c/y].

Aschwanden, M.J. and Peter, H. 2017, *The width distribution of loops and strands in the solar corona. - Are we hitting rock bottom ?* ApJ 840, 4, [7 c, 7 c/y].

Bourouaine, S. and Marsch, E. 2010, *Multi-strand coronal loop model and filter-ratio analysis*, ApJ 708, 1281, [2 c, 0.3 c/y].

Bradshaw, S.J. and Klimchuk, J.A. 2015, *Chromospheric nanoflares as a source of coronal plasma. II. Repeating nanoflares*, ApJ 811, 129, [7 c, 3 c/y].

Brooks, D.H., Warren, H.P., Ugarte-Urra, I., et al. 2013, *High spatial resolution observations of loops in the solar corona*, ApJ 772, L19, [47 c, 10 c/y].

Brooks, D.H., Reep, J.W., and Warren, H.P. 2016, *Properties and modeling of unresolved fine structure loops observed in the solar transition region by IRIS*, ApJ 826, L18, [4 c, 3 c/y].

Guarrasi, M., Reale, F., and Peres, G. 2010, *Coronal fuzziness modeled with pulse-heated multi-stranded loop systems*, ApJ 719, 576, [25 c, 3 c/y].

Jain, R. and Yashiro, S. 2002, *Filling factors and magnetic field strengths of nanoflare-heated coronal active regions: Yohkoh and MDI observations*, A&A 394, 1111, [6 c, 0.4 c/y].

Mendoza-Briceno, C.A., Erdelyi, R., and Di G. Sigaloti, L. 2002, *Coronal loop heating by random energy releases*, ApJ 579, L49, [27 c, 2 c/y].

Mulu-Moore, F.M., Winebarger, A.R., and Warren, H.P. 2011, *Can a long nanoflare storm explain the observed emission measure distributions in active region cores ?* ApJ 742, L6, [20 c, 3 c/y].

Patsourakos, S. and Klimchuk, J.A. 2005, *Coronal loop heating by nanoflares: The impact of the field-aligned distribution of the heating on loop observations*, ApJ 628, 1023, [42 c, 3 c/y].
Patsourakos, S. and Klimchuk, J.A. 2006, *Nonthermal spectral line broadening and the nanoflare model*, ApJ 647, 1452, [93 c, 8 c/y].
Peter, H., Bingert, S., Klimchuk, J.A., et al. 2013, *Structure of solar coronal loops: From miniature to large-scale*, A&A 556, A104, [52 c, 12 c/y].
Petrie, G.J.D. 2006, *Filamentary loop systems and spontaneous current sheets in the solar corona*, ApJSS 166, 378, [7 c, 0.6 c/y].
Reale, F. and Peres, G. 2000, *TRACE-derived temperature and emission measure profiles along long-lived coronal loops:* ApJ 528, L45, [80 c, 5 c/y].
Reale, F., Nigro, G., Malara, F., et al. 2005, *Modeling a coronal loop heated by MHD turbulence nanoflares*, ApJ 633, 489, [17 c, 1 c/y].
Reale, F. and Ciaravella, A. 2006, *Analysis of a multi-wavelength time-resolved observation of a coronal loop*, A&A 449, 1177, [15 c, 1 c/y].
Reale, F., Guarrasi, M., Testa, P., et al. 2011, *SDO discovers thin high temperature strands in coronal active regions*, ApJ 736, L16, [34 c, 5 c/y].
Sarkar, A. and Walsh, R.W. 2008, *Hydrodynamic simulation of a nanoflare-heated multistrand solar atmospheric loop*, ApJ 683, 516, [10 c, 1 c/y].
Sarkar, A. and Walsh, R.W. 2009, *EUV observational consequences of the spatial localization of nanoflare heating within a multistranded atmospheric loop*, ApJ 699, 1480, [5 c, 0.6 c/y].
Susino, R., Lanzafame, A.C., Lanza, A.F., et al. 2010, *Signatures of impulsive localized heating in the temperature distribution of multi-stranded coronal loops*, ApJ 709, 499, [19 c, 3 c/y].
Susino, R., Spadaro, D., Lanzafame, A.C., et al. 2013, *Properties of multistranded, impulsively heated hydrodynamic loop models*, A&A 552, A17, [0 c, 0 c/y].
Taroyan, Y., Bradshaw, S.J., and Doyle, J.G. 2006, *Nanoflare heating of coronal loops: hydrodynamic response and observational consequences*, A&A 446, 315, [23 c, 2 c/y].
Warren, H.P., Winebarger, A.R., and Hamilton, P.S. 2002, *Hydrodynamic modeling of active region loops*, ApJ 579, L41, [95 c, 6 c/y].
Warren, H.P., Winebarger, A.R., and Mariska, J.T. 2003, *Evolving active region loops observed with the TRACE. II. Time-dependent hydrodynamic simulations*, ApJ 593, 1174, [108 c, 7 c/y].
Winebarger, A.R., Schmelz, J.T., Warren, H.P., et al. 2011, *Using a differential emission measure and density measurements in an active region core to test a steady heating model*, ApJ 740, 2, [75 c, 12 c/y].

(9.4) Coronal Loops: Cross-Sectional Temperature

Aschwanden, M.J. 2002, *The differential emission measure distribution in the multiloop corona*, ApJ 580, L79, [25 c, 2 c/y].
Aschwanden, M.J. 2005, *Three criteria to discriminate between elementary and composite coronal loops*, ApJ 634, L193, [19 c, 2 c/y.
Aschwanden, M.J. and Nightingale, R.W. 2005, *Elementary loop structures in the solar corona analyzed from TRACE triple-filter images*, ApJ 633, 499, [108 c, 9 c/y].
Aschwanden, M.J. and Boerner, P. 2011, *Solar corona loop studies with the AIA. I. Cross-sectional temperature structure*, ApJ 732, 81, [79 c, 12 c/y].
Aschwanden, M.J., Boerner, P., Schrijver, C.J., et al. 2013, *Automated temperature and emission measure analysis of coronal loops and active regions observed with the AIA on SDO*, SoPh 283, 5, [78 c, 17 c/y].
Brooks, D.H., Warren, H.P., and Young, P.R. 2011, *EUV spectral line formation and the temperature structure of active region fan loops: Observations with Hinode/EIS and SDO/AIA*, ApJ 730, 85, 28 c, 4 c/y.

Cirtain, J.W., Del Zanna, G., DeLuca, E.E. et al. 2007, *Active region loops: Temperature measurements as a function of time from joint TRACE and SOHO CDS observations*, ApJ 655, 598, [31 c, 3 c/y.

Del Zanna, G. 2003, *Solar active regions: The footpoints of 1 MK loops*, A&A 406, L5, [30 c, 2 c/y].

Del Zanna, G. and Mason, H.E. 2003, *Solar active regions: SOHO/CDS and TRACE observations of quiescent coronal loops*, A&A 406, 1089, [130 c, 9 c/y].

Del Zanna, G. 2013, *The multi-thermal emission in solar active regions*, A&A 558, 73, [56 c, 12 c/y.

Landi, E. and Feldman, U. 2008, *The thermal structure of an active region observed outside the solar disk*, ApJ 672, 674, [26 c, 3 c/y].

Landi, E. and Klimchuk, J.A. 2010, *On the isothermality of solar plasmas*, ApJ 723, 320, [18 c, 2 c/y].

Martens, P.C.H., Cirtain, J.W., and Schmelz, J.T. 2002, *The inadequacy of temperature measurements in the solar corona through narrowband filter and line ratios*, ApJ 577, L115, [73 c, 5 c/y].

Nagata, S.I., Hara, H., Kano, R. et al. 2003, *Spatial and temporal properties of hot and cool coronal loops*, ApJ 590, 1095, [29 c, 2 c/y].

Patsourakos, S. and Klimchuk, J.A. 2007, *The cross-field thermal structure of coronal loops from triple-filter TRACE observations*, ApJ 667, 591, [19 c, 2 c/y].

Reale, F. and Landi, E. 2012, *The role of radiative losses in the late evolution of pulse-headed loops/strands*, A&A 543, A90, [15 c, 3 c/y].

Sasso, C., Andretta, V., Spandaro, D., et al. 2012, *Solar low-lying cool loops and their contribution to the transition region EUV output*, A&A 537, A150, [7 c, 1 c/y].

Schmelz, J.T., Scopes, R.T., Cirtain, J.W. et al. 2001, *Observational constraints on coronal heating models using CDS and SXT data*, ApJ 556, 896, [98 c, 6 c/y].

Schmelz, J.T. 2002, *Are coronal loops isothermal ?* ApJ 578, 161, [44 c, 3 c/y].

Schmelz, J.T., Beene, J.E., Nasraoui, K. et al. 2003, *The effect of background subtraction on the temperature of EIT coronal loops*, ApJ 599, 604, [37 c, 3 c/y].

Schmelz, J.T., Nasraoui, K., Richardson, V.L. et al. 2005, *All coronal loops are the same: Evidence to the contrary*, ApJ 627, L81, [21 c, 2 c/y].

Schmelz, J.T. and Martens, P.C.H. 2006, *Multithermal analysis of a SOHO/CDS coronal loop*, ApJ 636, L49, [34 c, 3 c/y].

Schmelz, J.T., Nasraoui, K., Del Zanna, G. et al. 2007, *CDS observations of isothermal and multithermal coronal loops*, ApJ 658, L119, [22 c, 2 c/y].

Schmelz, J.T., Scott, J., Rightmire, L.A. 2008, *May Day! Coronal loop temperatures from the Hinode EIS*, ApJ 684, 115, [12 c, 1 c/y].

Schmelz, J.T., Nasraoui, K., Rightmire, L.A. 2009, *Are coronal loops isothermal or multithermal ?* ApJ 691, 503, [24 c, 3 c/y].

Schmelz, J.T., Kimble, J.A., Jenkins, B.S. et al. 2010a, *AIA multithermal loop analysis: First results*, ApJ 725, L34, [16 c, 2 c/y].

Schmelz, J.T., Saar, S.H., Nasraoui, K. et al. 2010b, *Multi-stranded and multi-thermal solar coronal loops: Evidence from Hinode XRT and EIS data*, ApJ 723, 1180, [32 c, 4 c/y].

Schmelz, J.T., Worley, B.T., Anderson, D.J. et al. 2011a, *Isothermal and multithermal analysis of coronal loops observed with AIA. II. 211 A selected loops*, ApJ 739, 33, [18 c, 3 c/y].

Schmelz, J.T., Rightmire, L.A., Saar, S.H. et al. 2011b, *Warm and fuzzy: Temperature and density analysis of an Fe XV EIS Loop*, ApJ 738, 146, [17 c, 3 c/y].

Schmelz, J.T., Jenkins, B.S., Worley, B.T. et al. 2011c, *Isothermal and multithermal analysis of coronal loops observed with AIA*, ApJ 731, 49, [37 c, 6 c/y].

Schmelz, J.T., Pathak, S., Jenkins, B.S. et al. 2013, *Deeper by the Dozen: Understanding the cross-field temperature distributions of coronal loops*, ApJ 764, 53, [13 c, 3 c/y].

Testa, P., Peres, G., Reale, F., and Orlando, S. 2002, *Temperature and density structure of hot and cool loops derived from the analysis of TRACE data*, ApJ 580, 1159, [52 c, 4 c/y].

Tripathi, D., Mason, H.E., Dwivedi, B.N. et al. 2009, *Active region loops: Hinode/EIS observations*, ApJ 694, 1256, [87 c, 10 c/y].
Warren, H.P. and Warshall, A.D. 2002, *Temperature and density measurements in a quiet coronal streamer*, ApJ 571, 1999, [20 c, 1 c/y].
Warren, H.P. and Winebarger, A.R. 2003, *Density and temperature measurements in a solar active region*, ApJ 596, L113, [19 c, 1 c/y].
Warren, H.P., Ugarte-Urra, I., Doschek, G.A., et al. 2008, *Observations of active region loops with the EIS on Hinode*, ApJ 686, L131, [75 c, 8 c/y].
Warren, H.P., Mariska, J.T., and Doschek, G.A. 2013, *Observations of thermal flare plasma with the EUVE*, ApJ 770, 116, [22 c, 5 c/y].
Weber, M.A., Schmelz, J.T., DeLuca, E.E., et al. 2005, *Isothermal bias of the "filter ratio" method for observations of multithermal plasma*, ApJ 635, L101, [35 c, 3 c/y].

(9.5) Coronal Loops: Flows

Baker, D., Janvier, M., Démoulin, P., et al. 2017, *Apparent and intrinsic evolution of active region upflows*, SoPh 292, id.46.
Bethge, C., Beck, C., Peter, H. et al. 2012, *Siphon flow in a cool magnetic loop*, A&A 537, A130, [12 c, 2 c/y].
Brosius, J.W. 2005, *Mass flows in a disappearing sunspot plume*, ApJ 622, 1216, [19 c, 2 c/y].
Brosius, J.W. and Landi, E. 2005, *Properties of a sunspot plume observed with the CDS aboard the SOHO*, ApJ 632, 1196, [13 c, 1 c/y].
Byhring, H.S., Esser, R., and Lie-Svendsen, O. 2008, *The funnel geometry of open flux tubes in the low solar corona constrained by O VI and Ne VIII outflow*, ApJ 673, L91, [5 c, 0.5 c/y].
Del Zanna, G. 2008, *Flows in active region loops observed by Hinode EIS*, A&A 481, L49, [115 c, 12 c/y].
Démoulin, P., Baker, D., Mandrini, C.H. et al. 2013, *The 3-D geometry of active region upflows deduced from their limb-to-limb evolution*, SoPh 283, 341, [14 c, 3 c/y].
Doschek, G.A., Warren, H.P., Mariska, J.T., et al. 2008, *Flows and nonthermal velocities in solar active regions observed with the EIS on Hinode: A tracer of active region sources of heliospheric magnetic fields ?* ApJ 686, 1362, [115 c, 12 c/y].
Doyle, J.G., Taroyan, Y., Ishak, B. et al. 2006, *Study of a transient siphon flow in a cold loop*, A&A 452, 1075, [20 c, 2 c/y].
Feldman, U., Landi, E., and Curdt, W. 2003, *Nonthermal mass motions within the high-temperature plasma above a complex solar active region*, ApJ 585, 1087, [6 c, 0.4 c/y].
Hara, H., Watanabe, T., Harra, L.K. et al. 2008, *Coronal plasma motions near footpoints of active region loops revealed from spectroscopic observations with Hinode EIS*, ApJ 678, L67, [125 c, 13 c/y].
Kamio, S., Peter, H., Curdt, W., et al. 2011, *Continuous upflows and sporadic downflows observed in active regions*, A&A 532, A96, [26 c, 4 c/y].
Kano, R., Ueda, K., and Tsuneta, S. 2014, *Photospheric properties of warm EUV loops and hot X-ray loops*, ApJ 782, L32, [3 c, 1 c/y].
Killie, M.A., Lie-Svendsen, O., and Leer, E. 2005, *The helium abundance of quiescent coronal loops*, ApJ 632, L155, [7 c, 0.6 c/y].
Lenz, D.D. 2004, *Effects of flow on structure and abundances in multispecies solar coronal loops*, ApJ 604, 433, [7 c, 0.5 c/y].
Mahajan, S.M., Nikol'skaya, K.I., Shatashvili, N.L. et al. 2002, *Generation of flows in the solar atmosphere due to magnetofluid coupling*, ApJ 576, L161, [14 c, 1 c/y].
McIntosh, S.W., Tian, H., Sechler, M. et al. 2012, *On the Doppler velocity of emission line profiles formed in the "coronal Contraflow" that is the chromosphere-corona mass cycle*, ApJ 749, 60, [31 c, 6 c/y].

Orange, N.B., Chesny, D.L., Oluseyi, H.M. et al. 2013, *Direct observations of plasma upflows and condensation in a catastrophically cooling solar transition region loop*, ApJ 778, 90, [3 c, 0.7 c/y].
Patsourakos, S., Klimchuk, J.A., and Young, P.R. 2014, *Core and wing densities of asymmetric coronal spectral profiles: Implications for the mass supply of the solar corona*, ApJ 781, id. 58, [12 c, 3 c/y].
Raju, K.P., Chandrasekhar, T., and Ashok, N.M. 2011, *Analysis of coronal green line profiles: Evidence of excess blueshifts*, ApJ 736, 164, [5 c, 0.8 c/y].
Singh, J., Sakurai, T., Kiyoshi, I. et al. 2005, *Spectroscopic studies of solar corona VII. Formation of a coronal loop by evaporation*, SoPh 226, 201, [6 c, 0.5 c/y].
Su, J.T., Liu, Y., Shen, Y.D. et al. 2012, *Observation of high-speed outflows in coronal loops associated with photospheric magnetic field evolution*, ApJ 760, 82, [7 c, 1 c/y].
Tripathi, D., Mason, H.E., Dwivedi, B.N. et al. 2009, *Active region loops: Hinode EIS observations*, ApJ 694, 1256, [88 c, 10 c/y].
Tripathi, D., Mason, H.E., Del Zanna, G. et al. 2012a, *Observations of plasma upflow in a warm loop with Hinode/EIS*, ApJ 754, L4, [13 c, 2 c/y].
Tripathi, D., Mason, H.E., and Klimchuk, J.A. 2012b, *Active region moss: Doppler shifts from the Hinode/EIS observations*, ApJ 753, 37, [14 c, 2.5 c/y].
Ugarte-Urra, I. and Warren, H.P. 2011, *Temporal variability of active region outflows*, ApJ 730, 37, [32 c, 5 c/y].
Warren, H.P., Ugarte-Urra, I., Young, P., et al. 2011, *The temperature dependence of solar active region outflows*, ApJ 727, 58, [49 c, 8 c/y].
Winebarger, A.R., Warren, H., Van Ballegooijen, A. et al. 2002, *Steady flows detected in EUV loops*, ApJ 567, L89, [113 c, 7 c/y].

(9.6) Coronal Loops: Catastrophic Cooling

Ahn, K., Chae, J.C., Cho, K.S. et al. 2014, *Active region coronal rain event observed by the Fast Imaging Solar Spectrograph on the NST*, SoPh 289, 4117, [8 c, 1 c/y].
Antolin, P. and Rouppe van der Voort, L. 2012, *Observing the fine structure of loops through high-resolution spectroscopic observations of coronal rain with the CRISP instrument at the Swedish Solar Telescope (SST)*, ApJ 745, 152, [80 c, 15 c/y.
Antolin, P., Vissers, G., and Rouppe van der Voort, L. 2012, *On-Disk rain*, SoPh 280, 457, [27 c, 5 c/y].
Antolin, P., Vissers, G., Pereira, M.D., et al. 2015, *The multithermal and multi-stranded nature of coronal rain*, ApJ 806, 81, [34 c, 14 c/y].
Froment, C., Auchère, F., Bocchialini, K. et al. 2015, *Evidence for evaporation-incomplete condensation cycles in warm solar coronal loops*, ApJ 807, 158, [17 c, 7 c/y].
Froment, C., Auchére, F., Aulanier, G. et al. 2017, *Long-period intensity pulsations in coronal loops explained by thermal non-equilibrium cycles*, ApJ 835, 272, [5 c, 5 c/y].
Kohutova, P. and Verwichte, E. 2016, *Analysis of coronal rain observed by IRIS, Hinode/SOT, and SDO/AIA: Transverse oscillations, kinematics, and thermal evolution*, ApJ 827, 39, [7 c, 5 c/y].
Kohutova, P. and Verwichte, E. 2017a, *Dynamics of plasma condensations in a gravitationally stratified coronal loop*, A&A 602, A23, [2 c, 2 c/y].
Kohutova, P. and Verwichte, E. 2017b, *Excitation of vertical coronal loop oscillations by plasma condensations*, A&A 606, 120.
Mendoza-Briceno, C.A., Erdelyi, R., and Di G. Sigaloti, L. 2002, *Coronal loop heating by random energy releases*, ApJ 579, L49, [27 c, 2 c/y].
Müller, D.A.N., Hansteen, V.H., and Peter, H. 2003, *Dynamics of solar coronal loops. I. Condensation in cool loops and its effect on transition region lines*, A&A 411, 605, [100 c, 7 c/y.

Müller, D.A.N., Peter, H., and Hansteen, V.H. 2004, *Dynamics of solar coronal loops. II. Catastrophic cooling and high-speed downflows*, A&A 424, 289, [85 c, 6 c/y].

Oliver, R., Solar, R., Terradas, J. et al. 2016, *Dynamics of coronal rain and descending plasma blobs in solar prominences. II. Partially ionized case*, ApJ 818, 128, [7 c, 5 c/y].

Peter, H., Bingert, S., Kamio, S. et al. 2012, *Catastrophic cooling and cessation of heating in the solar corona*, A&A 537, A152, [13 c, 2 c/y].

Scullion, E., Rouppe van der Voort, L., Antolin, P. et al. 2016, *Observing the formation of flare-driven coronal rain*, ApJ 833, 184, [5 c, 3 c/y]

Verwichte, E. and Kohutova, P. 2017, *Excitation and evolution of vertically polarized transverse loop oscillations by coronal rain*, A&A 601, L2, [1 c, 1 c/y].

Verwichte, E., Antolin, P., Rowlands, G. et al. 2017, *Kinematics of coronal rain in a transversely oscillating loop: Ponderomotive force and rain-excited oscillations*, A&A 598, A57, [5 c, 5 c/y].

(9.7) Coronal Loops: Heating Function

Aschwanden, M.J., Newmark, J.S., Delaboudiniere, J.P., et al. 1999, *3-D stereoscopic analysis of solar active region loops. I. SOHO/EIT observations at temperatures of* $(1.0–1.5) \times 10^6$ *K*, ApJ 515, 842, [219 c, 12 c/y].

Aschwanden, M.J., Nightingale R.W., and Alexander, D. 2000, *Evidence for nonuniform heating of coronal loops inferred from multithread modeling of TRACE data*, ApJ 541, 1059, [234 c, 14 c/y].

Aschwanden, M.J. and Nitta, N. 2000, *The effect of hydrostatic weighting on the vertical temperature structure of the solar corona*, ApJ 535, L59, [35 c, 2 c/y].

Aschwanden, M.J. and Peter, H. 2017, *The width distribution of loops and strands in the solar corona. - Are we hitting rock bottom*, ApJ 840, 4, [7 c, 7 c/y].

Bradshaw, S.J. and Cargill, P.J. 2006, *Explosive heating of low-density coronal plasma*, A&A 458, 987, [58 c, 5 c/y].

Bradshaw, S.J. and Cargill, P.J. 2013, *The influence of numerical resolution on coronal density in hydrodynamic models of impulsive heating*, ApJ 770, 12, [36 c, 8 c/y].

Brooks, D.H., Warren, H.P., Ugarte-Urra, I. et al. 2013, *High spatial resolution observations of loops in the solar corona*, ApJ 772, L19, [47 c, 10 c/y].

Chae, J.C., Poland, A.I., and Aschwanden, M.J. 2002, *Coronal loops heated by MHD turbulence. I. A model of isobaric Quiet-Sun loops with constant cross sections*, ApJ 581, 726, [14 c, 1 c/y].

Guarrasi, M., Reale, F., and Peres, G. 2010, *Coronal fuzziness modeled with pulse-heated multi-heated multi-stranded loop systems*, ApJ 719, 576.

Klimchuk, J.A. 2006, *On solving the coronal heating problem*, SoPh 234, 41, [471 c, 41 c/y].

Klimchuk, J.A. 2009, *Coronal loop models and those annoying observations ?* (Keynote), in "The Second Hinode Science Meeting", ASP Conf. Ser. Vol. 415, (eds. B.Lites et al.), p.221.

Lenz, D.D., DeLuca, E.E., Golub, L., et al. 1999, *Temperature and emission-measure profiles along long-lived coronal loops observed with the TRACE*, ApJ 517, L155, [145 c, 8 c/y].

Mikic, Z., Lionello, R., Mok, Y., et al. 2013, *The importance of geometric effects in coronal loop models*, ApJ 773, 94, [34 c, 10 c/y].

Mulu-Moore, F.M., Winebarger, A.R., Warren, H.P., et al. 2011, *Determining the structure of solar coronal loops using their evolution*, ApJ 733, 59, [23 c, 4 c/y].

Patsourakos, S. and Klimchuk, J.A. 2006, *Nonthermal spectral line broadening and the nanoflare model*, ApJ 647, 1452, [93 c, 8 c/y].

Peter, H., Bingert, S., Klimchuk, J.A., et al. 2013, *Nanoflare statistics in an active region 3D MHD coronal model*, AA 556, A104, [23 c, 5 c/y].

Reale, F. 2002, *More on the determination of the coronal heating function from Yohkoh data*, ApJ 580, 566, [38 c, 2 c/y].

Rosner, R., Tucker, W.H., and Vaiana, G.S. 1978, *Dynamics of the quiescent solar corona*, ApJ 220, 643, [1301 c, 33 c/y].
Serio, S., Peres, G., Vaiana, G.S., et al. 1981, *Closed coronal structures. II. Generalized hydrostatic model*, ApJ 243, 288, [272 c, 7 c/y].
Testa, P., Peres, G., and Reale, F. 2005, *Emission measure distribution in loops impulsively heated at the footpoints*, ApJ 622, 695, [31 c, 2 c/y].
Warren, H.P., Winebarger, A.R., and Hamilton, P.S. 2002, *Hydrodynamic modeling of active regions*, ApJ 579, L41, [95 c, 6 c/y].
Warren, H.P., Winebarger, A.R., and Mariska, J.T. 2003, *Evolving active region loops observed with the TRACE. II. Time-dependent hydrodynamic simulations*, ApJ 593, 1174, [108 c, 7 c/y].
Warren, H.P., Kim, D.M., DeGiorgi, M., et al. 2010a, *Modeling evolving coronal loops with observations from STEREO, Hinode, and TRACE*, ApJ 713, 1095, [17 c, 2 c/y].
Warren, H.P., Winebarger, A.R., and Brooks, D.H. 2010b, *Evidence for steady heating: Observations of an active region core with Hinode and TRACE*, ApJ 711, 228, [51 c, 7 c/y].
Winebarger, A.R., Warren, H.P., and Seaton, D.B. 2003, *Evolving active region loops observed with the TRACE. I. Observations*, ApJ 593, 1164, [88 c, 6 c/y].

(9.8) Coronal Loops: The 0-D EBTEL Code

Antiochos, S.K., MacNeice, P.J., Spicer, D.S., et al. 1999, *The dynamic formation of prominence condensations*, ApJ 512, 985, [145 c, 8 c/y].
Aschwanden, M.J. and Tsiklauri, D. 2009, *The hydrodynamic evolution of impulsively heated coronal loops: Explicit analytical approximations*, ApJSS 185, 171, [15 c, 2 c/y].
Bradshaw, S.J. and Klimchuk, J.A. 2011, *What dominates the coronal emission spectrum during the cycle of impulsive heating and cooling ?* ApJSS 194, 26., [53 c, 8 c/y]
Cargill, P.J. 1994, *Some implications of the nanoflare concept*, ApJ 422, 381, [188 c, 8 c/y].
Cargill, P.J., Bradshaw, S.J., and Klimchuk, J.A. 2012a, *Enthalpy-based thermal evolution of loops. II. Improvements to the model*, ApJ 752, 161, [43 c, 8 c/y].
Cargill, P.J., Bradshaw, S.J., and Klimchuk, J.A. 2012b, *Enthalpy-based thermal evolution of loops. III. Comparison of 0-D models*, ApJ 758, 5, [24 c, 4 c/y].
Fisher, G.H. and Hawley, S.L. 1990, *An equation for the evolution of solar and stellar flare loops*, ApJ 357, 243, [67 c, 2 c/y].
Klimchuk, J.A., Patsourakos, S., and Cargill, P.J. 2008, *Highly efficient modeling of dynamic coronal loops*, ApJ 682, 1351, [153 c, 16 c/y].
Kopp, R.A. and Poletto, G. 1993, *Coronal heating by nanoflares: Individual events and global energetics*, ApJ 418, 496, [39 c, 2 c/y].
Kuin, N.P.M. and Martens, P.C.H. 1982, *On the thermal stability of hot coronal loops. The coupling between chromosphere and corona*, A&A 108, L1, [68 c, 2 c/y].
Raftery, C.L., Gallagher, P.T., Milligan, R.O., et al. 2009, *Multi-wavelength observations and modelling of a canonical solar flare*, ApJ 494, 1127, [44 c, 5 c/y].
Ugarte-Urra, I. and Warren, H.P. 2014, *Determining heating timescales in solar active region cores from AIA/SDO Fe XVIII images*, ApJ 783, 12, [14 c, 4 c/y].
Viall, N.M. and Klimchuk, J.A. 2012, *Evidence for widespread cooling in an active region observed with the SDO/AIA*, ApJ 753, 35, [60 c, 11 c/y].

(9.9) Coronal Loops: 1-D Hydrodynamics

Antiochos, S.K., MacNeice, P.J., Spicer, D.S., et al. 1999, *The dynamic formation of prominence condensations*, ApJ 512, 985, [145 c, 8 c/y].
Aschwanden, M.J. and Tsiklauri, D. 2009, *The hydrodynamic evolution of impulsively heated coronal loops: Explicit analytical approximations*, ApJS 185, 171, [15 c, 2 c/y].
Aschwanden, M.J. and Shimizu, T. 2013, *Multi-wavelength observations of the spatio-temporal evolution of solar flares with AIA/SDO. II. Hydrodynamic scaling laws and thermal energies*, ApJ 776, 132, [14 c, 3 c/y].
Bradshaw, S.J. 2008, *A re-interpretation of the energy balance in active region loops following new results from Hinode EIS*, A&A 486, L5.
Bradshaw, S.J. and Mason, H.E. 2003, *A self-consistent treatment of radiation in coronal loop modelling*, A&A 401, 699, [60 c, 4 c/y].
Dudik, J., Dzifcakova, E., Karlicky, M., et al. 2009, *Analytical model of static coronal loops*, A&A 502, 957, [2 c, 0.2 c/y].
Jakimiec,J., Sylwester,B., Sylwester,J., et al. 1992, *Dynamics of flaring loops. II. Flare evolution in the density-temperature diagram*, A&A 253, 269, [93 c, 4 c/y].
Kuin, N.P.M. and Martens, P.C.H. 1982, *On the thermal stability of hot coronal loops. The coupling between chromosphere and corona*, A&A 108, L1, [68 c, 2 c/y].
Landi, E. and Landini, M. 1999, *Radiative losses of optically thin coronal plasmas*, A&A 347, 401, [46 c, 2 c/y].
Landini, M. and Landi, E. 2002, *Models for solar magnetic loops. I. A simple theoretical model and diagnostic procedure*, A&A 383, 653, [9 c, 0.6 c/y].
Martens, P.C.H. 2010, *Scaling laws and temperature profiles for solar and stellar coronal loops with nonuniform heating*, ApJ 714, 1290, [23 c, 3 c/y].
Rosner, R., Tucker, W.H., and Vaiana, G.S. 1978, *Dynamics of the quiescent solar corona*, ApJ 220, 643, [1301 c, 33 c/y].
Serio, S., Peres, G., Vaiana, G.S., et al. 1981, *Closed coronal structures. II. Generalized hydrostatic model*, ApJ 243, 288, [272 c, 7 c/y].
Sylwester, B., Sylwester, J., Serio, S. et al. 1993, *Dynamics of flaring loops. III. Interpretation of flare evolution in the emission measure-temperature diagram*, A&A 582, 486, [57 c, 2 c/y].

(9.10) Coronal Loops: Magnetic Modeling

Amari, T., Boulmezaoud, T.Z., and Aly, J.J. 2006, *Well posed reconstruction of the solar coronal magnetic field*, A&A 446, 691, [94 c, 8 c/y].
Aschwanden, M.J. and Sandman, A.W. 2010, *Bootstrapping the coronal magnetic field with STEREO: Unipolar potential field modeling*, Astron. J. 140, 723, [23 c, 3 c/y].
Aschwanden, M.J., Wuelser, J.P., Nitta, N.V. et al. 2012, *First 3-D reconstruction of coronal loops with the STEREO A+B spacecraft. IV. Magnetic modeling with twisted force-free fields*, ApJ 756, 124, [21 c, 4 c/y].
Aschwanden, M.J. 2013a, *Nonlinear force-free magnetic field fitting to coronal loops with and without stereoscopy*, ApJ 763, 115, [17 c, 4 c/y].
Aschwanden, M.J. 2013b, *A nonlinear force-free magnetic field approximation suitable for fast forward-fitting to coronal loops. I. Theory*, SoPh 287, 323, [17 c, 4 c/y].
Aschwanden, M.J. and Malanushenko, A. 2013, *A nonlinear force-free magnetic field approximation suitable for fast forward-fitting to coronal loops. II. Numeric Code and Tests*, SoPh 287, 345, [20 c, 4 c/y].
Aschwanden, M.J. 2013c, *A nonlinear force-free magnetic field approximation suitable for fast forward-fitting to coronal loops. III. Free energy*, SoPh 287, 369, [15 c, 3 c/y].
Aschwanden, M.J., Xu, Y., and Jing, J. 2014, *Global energetics of solar flares. I. Magnetic energies*, ApJ 797, 50, [26 c, 7 c/y].

Aschwanden, M.J. 2016, *The vertical-current approximation nonlinear force-free field code - Description, performance, tests, and measurements of magnetic energies dissipated in solar flares*, ApJSS 224, 25, [8 c, 5 c/y].

Aschwanden, M.J., Reardon, K., and Jess, D.B. 2016, *Tracing the chromosphere and coronal magnetic field with AIA, IRIS, IBIS, and ROSA data*, ApJ 826, 61, [5 c, 3 c/y].

Bobra, M.G., van Ballegooijen, A.A. and DeLuca, E.E. 2008, *Modeling nonpotential fields in solar active regions*, ApJ 672, 1029, [79 c, 8 c/y].

De Rosa, M.L., Schrijver, C.J., Barnes, G., et al. 2009, *A critical assessment of nonlinear force-free field modeling of the solar corona for active region 10953*, ApJ 696, 1780, [230 c, 27 c/y].

Flyer, N., Fornberg, B., Thomas, S. et al. 2004, *Magnetic field confinement in the solar corona. I. Force-free magnetic fields*, ApJ 606, 1210, [46 c, 3 c/y].

Metcalf, T.R., Jiao, L., Uitenbroek, H., et al. 1995, *Is the solar chromospheric magnetic field force-free ?* ApJ 439, 474, [212 c, 9 c/y].

Metcalf, T.R., DeRosa, M.L., Schrijver, C.J. et al. 2008, *Nonlinear force-free modeling of coronal magnetic fields. II. Modeling a filament arcade and simulated chromospheric and photospheric vector fields*, SoPh 247, 269, [151 c, 16 c/y].

Sandman,A W., Aschwanden, M.J., Derosa, M.L., et al. 2009, *Comparison of STEREO/ EUVI loops with potential magnetic field models*, SoPh 259, 1, [31 c, 4 c/y].

Sandman, A.W. and Aschwanden, M.J. 2011, *A new method for modeling the coronal magnetic field with STEREO and submerged dipoles*, SoPh 270, 503, [17 c, 3 c/y].

Schrijver, C.J., DeRosa, M.L., Metcalf, T.R. et al. 2006, *Nonlinear force-free modeling of coronal magnetic fields Part I: A quantitative comparison of methods*, SoPh 235, 161, [215 c, 19 c/y].

Song, M.T., Fang, C., Tang, Y.H. et al. 2006, *A new and fast way to reconstruct a nonlinear force-free field in the solar corona*, ApJ 649, 1084, [39 c, 3 c/y].

Titov, V.S., Török, T., Mikic, Z., et al. 2014, *A method of embedding circular force-free flux ropes in potential magnetic fields*, ApJ 790, 163, [15 c, 4 c/y].

Van Ballegooijen, A.A. 2004, *Observations and modeling of a filament on the Sun*, ApJ 612, 519, [151 c, 12 c/y].

Van Ballegooijen, A.A., DeLuca, E.E., Squires, K. et al. 2007, *Modeling magnetic flux ropes in the solar atmosphere*, Atmos. Terr. Phys. 69, 24, [12 c, 1 c/y].

Wheatland, M.S., Sturrock, P.A., and Roumeliotis, G. 2000, *An optimization approach to reconstructing force-free fields*, ApJ 540, 1150, [250 c, 14 c/y].

Wiegelmann, T. 2004, *Optimization code with weighting function for the reconstruction of coronal magnetic fields*, SoPh 219, 87, [276 c, 20 c/y].

Wiegelmann, T., Inhester, B., and Sakurai, B. 2006, *Preprocessing of vector magnetograph data for a nonlinear force-free magnetic field reconstruction*, SP 223, 215, [217 c, 19 c/y].

Wiegelmann, T. 2007, *Computing nonlinear force-free coronal magnetic fields in spherical geometry*, SoPh 240, 227, [46 c, 4 c/y].

Wiegelmann, T. and Inhester, B. 2010, *How to deal with measurement errors and lacking data in nonlinear force-free magnetic field modeling ?* A&A 516, A107, [64 c, 9 c/y].

Wiegelmann, T., Thalmann, J.K., Inhester, B. et al. 2012, *How should one optimize nonlinear force-free coronal magnetic field extrapolations from SDO/HMI vector magnetograms*, SoPh 281, 37, [66 c, 12 c/y].